JACS
JOURNAL OF THE AMERICAN CHEMICAL SOCIETY
pubs.acs.org/JACS
Article

Simultaneous Elucidation of Solid and Solution Manganese Environments via Multiphase *Operando* Extended X-ray Absorption Fine Structure Spectroscopy in Aqueous Zn/MnO_2 Batteries

Daren Wu,[▽] Lisa M. Housel,[▽] Steven T. King, Zachary R. Mansley, Nahian Sadique, Yimei Zhu, Lu Ma, Steven N. Ehrlich, Hui Zhong, Esther S. Takeuchi, Amy C. Marschilok, David C. Bock, Lei Wang, and Kenneth J. Takeuchi*

Cite This: *J. Am. Chem. Soc.* 2022, 144, 23405−23420
Read Online
ACCESS | Metrics & More | Article Recommendations | Supporting Information

ABSTRACT: Aqueous Zn/MnO_2 batteries (AZMOB) with mildly acidic electrolytes hold promise as potential green grid-level energy storage solutions for clean power generation. Mechanistic understanding is critical to advance capacity retention needed by the application but is complex due to the evolution of the cathode solid phases and the presence of dissolved manganese in the electrolyte due to a dissolution−deposition redox process. This work introduces *operando* multiphase extended X-ray absorption fine structure (EXAFS) analysis enabling simultaneous characterization of both aqueous and solid phases involved in the Mn redox reactions. The methodology was successfully conducted in multiple electrolytes ($ZnSO_4$, $Zn(CF_3SO_3)_2$, and $Zn(CH_3COO)_2$) revealing similar manganese coordination environments but quantitative differences in distribution of Mn^{n+} species in the solid and solution phases. Complementary Raman spectroscopy was utilized to identify the less crystalline Mn-containing products formed under charge at the cathodes. This was further augmented by transmission electron microscopy (TEM) to reveal the morphology and surface condition of the deposited solids. The results demonstrate an effective approach for bulk-level characterization of poorly crystalline multiphase solids while simultaneously gaining insight into the dissolved transition-metal species in solution. This work provides demonstration of a useful approach toward gaining insight into complex electrochemical mechanisms where both solid state and dissolved active materials are important contributors to redox activity.

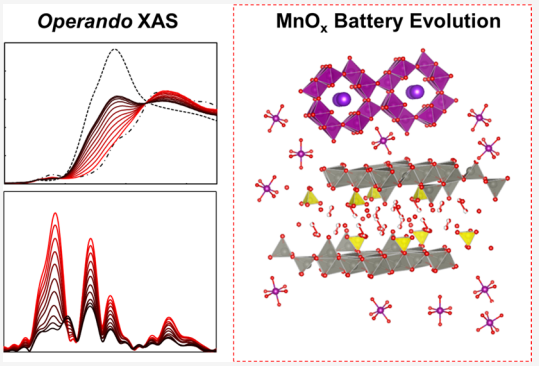

INTRODUCTION

Power systems are undergoing transformation globally driven by operational, environmental, policy, and investment considerations. Widespread integration of renewable energy has become an important subject of scientific and engineering investigation to achieve cleaner power systems. Due to the inherent intermittency of sources such as wind and solar-generated power, effective and scalable energy storage is required for their widespread adoption. Reversible aqueous Zn/MnO_2 batteries (AZMOBs) have emerged as a promising grid-scale storage alternative due to safety and low cost compared to commercialized Li-ion batteries.[1−3]

First proposed with a $ZnSO_4$ electrolyte in 1986,[4] AZMOBs with mildly acidic electrolytes have gained renewed research attention in recent years motivated by a need to fully understand its charge storage mechanism to improve its efficiency and cycling life.[5−7] Notably, studies of Mn redox in AZMOBs with different mildly acidic electrolytes have yielded varying conclusions. The findings can be divided into several general reaction routes: Zn^{2+}/H^+ insertion,[8−11] Zn^{2+}/H^+ insertion induced MnO_2-Zn_xMnO_y/MnOOH conversion,[8,9,11−19] and Mn^{n+} dissolution−deposition.[20−30] Among these studies, X-ray diffraction (XRD) methods have been employed to probe the cathode material either *ex situ* post-cycling or *operando*,[6,8,9,12−15,17−19] leading to the identification of insertion and conversion mechanisms for MnO_2 including its ability to serve as a Zn^{2+}/H^+ host. However, as suggested by prior TEM studies,[22,23] the deposited MnO_x charge product is poorly crystalline, making powder X-ray diffraction results challenging to interpret.

Several research efforts have proposed a dissolution−deposition process based on evidence provided by inductively coupled plasma-optical emission spectroscopy (ICP-OES),[21]

Received: September 6, 2022
Published: December 13, 2022

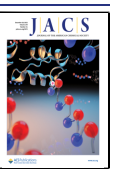

ACS Publications
© 2022 The Authors. Published by American Chemical Society

https://doi.org/10.1021/jacs.2c09477
J. Am. Chem. Soc. 2022, 144, 23405−23420

TEM,[14,23] or *operando* electrolyte pH tracking.[25] Recently, the use of *operando* synchrotron X-ray fluorescence mapping (XFM) enabled direct experimental evidence of reversible faradic MnO_2 dissolution−deposition as the dominant Mn redox reaction in $ZnSO_4$ electrolyte.[22] The XFM method enabled quantitative determination of the Mn^{n+} dissolution−deposition reaction and the ability to couple the findings with the observed electrochemistry. However, the XFM method did not provide structural information or insight into the coordination environment evolution within the solid positive electrode or the electrolyte.

While $ZnSO_4$ is a commonly studied mildly acidic Zn^{2+} electrolyte applicable for AZMOBs, other zinc salts with bulky anions such as triflate ($[CF_3SO_3]^-$) are of interest for improving the stability of both the Zn anode and manganese oxide-based cathodes.[15,16] Previous reports indicate that acetate ($[CH_3COO]^-$) can facilitate reversible $MnO_{2(s)} \rightleftharpoons Mn_{(aq)}^{2+}$ conversion by a coordination effect, where the $[CH_3COO]^-$ anion binds to $MnO_{2(s)}$ surface and H^+.[31−33] Recent TEM analyses[23] and *operando* pH studies[25,34] have suggested that reversible Mn dissolution−deposition may occur in AZMOBs with $Zn(CF_3SO_3)_2$ or $Zn(CH_3COO)_2$ electrolytes, similar to that in $ZnSO_4$ electrolyte. However, detailed studies providing temporally resolved bulk characterization and phase identification at the systems level are still lacking.

Herein, we demonstrate a synchrotron-based X-ray absorption spectroscopy (XAS) characterization method with resolved *operando* X-ray absorption near-edge spectroscopy (XANES) and extended X-ray absorption fine structure (EXAFS). This study utilized a combined XANES and multiphase EXAFS fitting method for the quantification of coexisting aqueous and poorly crystalline solid phases in AZMOBs acquired during the electrochemical function of the battery. This method allowed the characterization of both the aqueous and poorly crystalline phases involved in the Mn redox reactions in AZMOBs with $ZnSO_4$, $Zn(CF_3SO_3)_2$, or $Zn(CH_3COO)_2$ electrolyte. Combined with *ex situ* synchrotron XRD, TEM, and Raman spectroscopy, we characterize the Mn dissolution−deposition reactions with temporally resolved cathode/electrolyte at the bulk level during cycling and structure determination using local probes. The results provide insight into the reversible Mn dissolution−deposition for AZMOBs with mildly acidic electrolytes and demonstrate a methodology to simultaneously characterize both solid phase and dissolved transition-metal ions.

EXPERIMENTAL SECTION

Materials Synthesis. α-MnO_2 nanorods were synthesized via a method adopted from previous reports.[35,36] $KMnO_4$ was dissolved in hydrochloric acid and then heated to 140 °C for 36 h in a hydrothermal autoclave. The resultant product was washed with deionized water, vacuum-dried, and calcined at 300 °C in air for 6 h before use.

Material Characterization. X-ray diffraction (XRD) of the pristine material was collected at the 28-ID-2 XPD beamline of the National Synchrotron Light Source II (NSLS-II) at Brookhaven National Laboratory with a wavelength of 0.1847 Å. Rietveld refinement of the obtained patterns was performed with the GSAS-II software package.[37] Water content of the pristine material was measured by thermogravimetric analysis (TGA), and the potassium-manganese ratio of the material was estimated by inductively coupled plasma-optical emission spectroscopy (ICP-OES) using a Thermo Fisher iCap 6300 series instrument.

Electrolyte Conductivity, Viscosity, and pH Measurements. Conductivity and pH measurements of the 1 M $ZnSO_4$, 1 M $Zn(CF_3SO_3)_2$, and 1 M $Zn(CH_3COO)_2$ electrolytes were performed using a Mettler Toledo SevenExcellence series with conductivity and pH modules using InLab Expert Pro-ISM pH electrode and InLab 731-ISM conductivity probe at room temperature. The viscosity of the electrolytes was measured using a Brookfield LVDV-II+ viscometer using six temperatures between 20 and 32 °C. The viscosity at 25 °C was obtained by fitting the Arrhenius model to our measurement results.

Electrode Preparation and Electrochemical Measurements. The as-synthesized material and multiwall carbon nanotubes (MWCNT, Cheaptubes) were dispersed in a mass ratio of 7:3 and filtered to obtain a 3D-porous electrode. Electrochemical cells were assembled with the α-MnO_2/CNT cathode, glass fiber separator, zinc metal anode, and aqueous 1 M $ZnSO_4$, 1 M $Zn(CF_3SO_3)_2$, or 1 M $Zn(CH_3COO)_2$ electrolytes. Galvanostatic cycling tests were conducted using a BioLogic potentiostat at a current of 100 mA/g between 0.9 and 1.8 V vs Zn. Cyclic voltammetry tests were conducted with a BioLogic potentiostat at a scan rate of 0.1 mV/s between 0.9 and 1.8 V vs Zn. Electrodes in charged and discharged states were recovered, rinsed with deionized water, and dried. Zn−Zn symmetric cells were assembled in coin-type configuration with two Zn metal electrodes; a glass fiber separator; and 1 M $ZnSO_4$, 1 M $Zn(CF_3SO_3)_2$, or 1 M $Zn(CH_3COO)_2$ electrolytes, cycled between −0.5 and 0.5 V at a current density of 1 mA/cm^2.

Post-Electrochemical *Ex Situ* Characterizations. Recovered discharged or charged cathodes were placed between Kapton tapes for synchrotron X-ray diffraction characterization at the 28-ID-2 XPD beamline of the NSLS-II at Brookhaven National Laboratory. Transmission electron microscopy (TEM) and scanning TEM (STEM) of the cathodes after the initial charge in $ZnSO_4$, $Zn(CF_3SO_3)_2$, and $Zn(CH_3COO)_2$ electrolytes and the cathode cycled to the first discharge in $ZnSO_4$ electrolyte were done with a JEOL ARM200CF operated at 200 kV. The microscope is equipped with CEOS GmbH double-spherical aberration correctors along with a GIF Quantum ER energy filter with dual electron energy loss spectroscopy (EELS) capability. EELS spectra were collected using a Gatan K3 IS detector and data analysis includes zero-loss calibration, power-law background subtraction, and Fourier log-ratio deconvolution to remove plural scattering effects. EELS maps are generated using linear least-squares peak fitting of "surface" and "bulk" references determined away from the interface. Discharged samples were examined using a JEOL 2100 operated at 200 kV. Other recovered cathodes cycled to the first discharge and first charge were examined by confocal Raman microscopy. 2D 60 × 60 μm^2 Raman maps (5 μm step, 13 × 13 pixel^2) of each electrode were obtained using a Horiba XploRA confocal Raman microscope equipped with a 532 nm laser, resulting in a total of 169 spectra per electrode. A similar map was also obtained of an as-prepared electrode. Spectra were collected in the range of 200−1100 cm^{-1} using a 20× magnification objective. Non-negative matrix factorization (NMF) was used to unmix discrete Raman spectral signal components in the acquired mapping datasets for qualitative identification of chemical species and quantitative analysis of their relative abundances on each electrode.[38−40] Additional discharged/charged cathodes were prepared for *ex situ* XRD analysis on Rigaku Smartlab Diffractometer with Cu Kα radiation, the discharged samples were soaked in 10% acetic acid for 30 min before being rinsed with DI water to remove zinc hydroxy sulfate (acetate or triflate).

Operando X-ray Absorption Spectroscopy Characterization. *Operando* Mn K-edge X-ray absorption spectroscopy (XAS), which includes X-ray absorption near-edge structure (XANES) and extended X-ray absorption fine structure (EXAFS) measurements, were collected at 7-BM of the NSLS-II. Custom cells containing as-prepared cathodes, glass fiber separators, zinc anodes, and aqueous 1 M $ZnSO_4$, 1 M $Zn(CF_3SO_3)_2$, or 1 M $Zn(CH_3COO)_2$ electrolytes were used. Aqueous Mn standards containing pure CNT cathodes, zinc anodes, and glass fiber separators with 1 M $ZnSO_4$ + 0.5 M $MnSO_4$, 1 M $Zn(CF_3SO_3)_2$ + 0.5 M $Mn(CF_3SO_3)_2$, or 1 M

https://doi.org/10.1021/jacs.2c09477
J. Am. Chem. Soc. 2022, 144, 23405−23420

$Zn(CH_3COO)_2$ + 0.5 M $Mn(CH_3COO)_2$ electrolytes were also collected. All spectra were aligned, merged, and normalized using Athena.[41] Linear combination fitting (LCF) of the XANES region in all spectra was performed in Athena, utilizing pristine scans of the *operando* cells and the aqueous Mn standards for corresponding electrolytes as fitting standards to obtain aqueous and solid Mn weight fractions. Part of the EXAFS spectra were fitted with theoretical models calculated via FEFF6[42] within the *k*-range of 3−12 $Å^{-1}$ using a Hanning window (dk = 2) in *k*, k^2, and k^3 *k*-weights simultaneously. The fit was conducted over an *R*-range of 1−3.4 Å to encompass the Mn−O and Mn−Mn coordination shells. Pristine scans of each *operando* cell and aqueous Mn standards were fit first to obtain amplitude reduction factors used in the fitting of the remaining *operando* scans. Phase weight fraction was introduced into each fit to achieve multiphase fitting and account for different Mn phases in the *operando* cells.

RESULTS AND DISCUSSION

***Ex Situ* Characterization.** Synchrotron X-ray diffraction was collected for the as-synthesized α-MnO_2 powder followed by Rietveld refinement (Figure S1a). The cryptomelane-type α-MnO_2 (*I*4/*m* space group, PDF # 00-020-0908) consists of a 2 × 2 MnO_6 tunneled framework with K^+ ions partially occupying the tunnel center. ICP-OES determined the K/Mn ratio as 0.92:8 and water content estimated via TGA gave a final chemical formula of $K_{0.92}Mn_8O_{16}{\cdot}0.45H_2O$. The measured conductivity/pH/viscosity values of the electrolytes at room temperature (25 °C) are listed in Table 1.

Table 1. Measured pH/Conductivity/Viscosity Values of the Three 1 M Electrolytes along with the First Discharge Voltage Plateau of the Corresponding Zn/Mn Cells

property	1 M $ZnSO_4$	1 M $Zn(CF_3SO_3)_2$	1 M $Zn(CH_3COO)_2$
1st discharge voltage (V vs Zn)	1.22	1.04	1.14
pH	4.97	5.07	5.80
conductivity ($\mu S{\cdot}cm^{-1}$)	4.34 × 10^4	6.14 × 10^4	1.66 × 10^4
viscosity (cP)	2.05	2.45	2.14

The full viscosity measurement and fitting results are shown in Figure S15. Representative galvanostatic cycling voltage profiles of Zn/MnO_2 batteries with three different electrolytes over the first cycle are shown in Figure S1b. The $ZnSO_4$ and $Zn(CH_3COO)_2$ cells delivered ∼200 and ∼150 mAh/g on discharge and charge, respectively, while the $Zn(CF_3SO_3)_2$ cell delivered ∼230 mAh/g upon discharge and ∼180 mAh/g upon charge. The capacity differences observed for the three electrolyte systems could partially be attributed to the voltage limit upon discharge, which was chosen to be 0.9 V for consistency across different systems and to avoid the hydrogen evolution reaction. While the $Zn(CF_3SO_3)_2$ cell has a single-plateau discharge profile, a rapid voltage drop near the end suggests completion of electrochemical reaction. However, for $ZnSO_4$ and $Zn(CH_3COO)_2$ cells, which both have a two-plateau voltage profile during discharge, the second discharge plateau seemed to be cut short at 0.9 V, suggesting that the discharge reaction might not have been completed; therefore, lower discharge capacities were reasonable.

The α-MnO_2 cathodes cycled to the first discharge and first charge in the different electrolytes were characterized using synchrotron-based XRD (Figure 1). Upon discharge, intense peaks emerged below 1° in all cycled cathodes (red dashed box in Figure 1a), indicating the formation of new phases. For the $ZnSO_4$ system, this new phase was identified as layered zinc hydroxy sulfate hydrate (ZHS) with varying water content as a product formed due to local pH change within the system.[22] Previous reports have indicated that for $Zn(CH_3COO)_2$ and $Zn(CF_3SO_3)_2$ systems, similar layered zinc hydroxide hydrate paired with either CH_3COO^- anion or $CF_3SO_3^-$ anion forms upon discharge.[23,43,44] Thus, the XRD patterns of the discharged samples indicate the formation of either zinc hydroxy sulfate hydrate ($Zn_4SO_4(OH)_6{\cdot}xH_2O$, ZHS), zinc hydroxy-triflate hydrate ($Zn_5(OH)_8(CF_3SO_3)_2{\cdot}xH_2O$, ZHT) or zinc hydroxy-acetate hydrate ($Zn_5(OH)_8(CH_3COO)_2{\cdot}xH_2O$, ZHA) as a product in the corresponding electrolyte systems, with the most intense peaks below 1° corresponding to the (001) planes. Notably, the prime layering (001) peaks of ZHA and ZHT are at a lower angle than that of the ZHS,

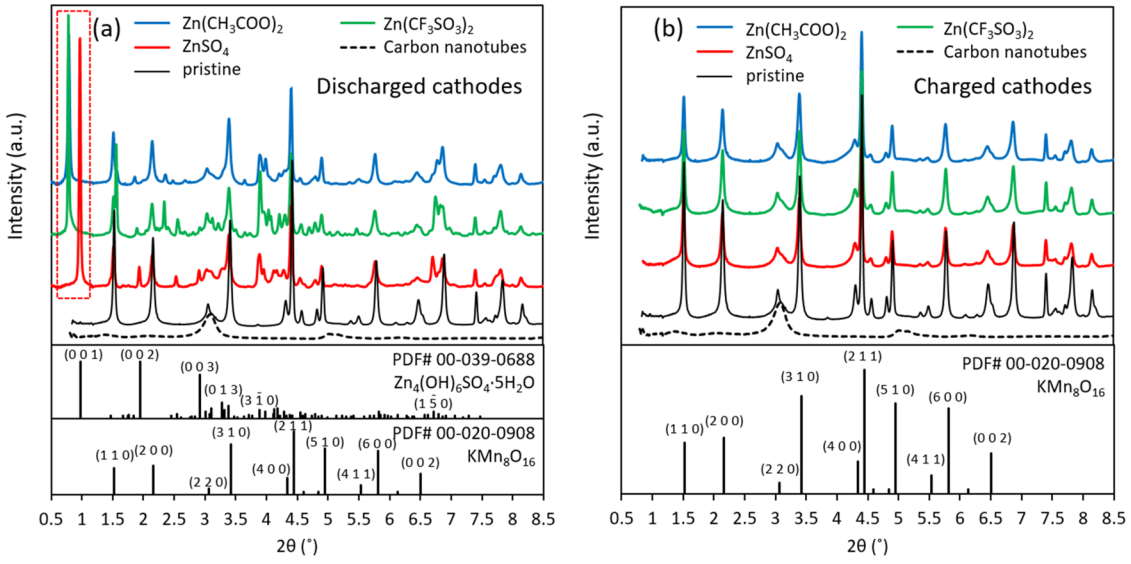

Figure 1. Synchrotron XRD patterns of (a) discharged and (b) charged cathodes cycled in $ZnSO_4$, $Zn(CF_3SO_3)_2$, or $Zn(CH_3COO)_2$ electrolytes along with pristine electrode and carbon nanotubes.

https://doi.org/10.1021/jacs.2c09477
J. Am. Chem. Soc. 2022, 144, 23405−23420

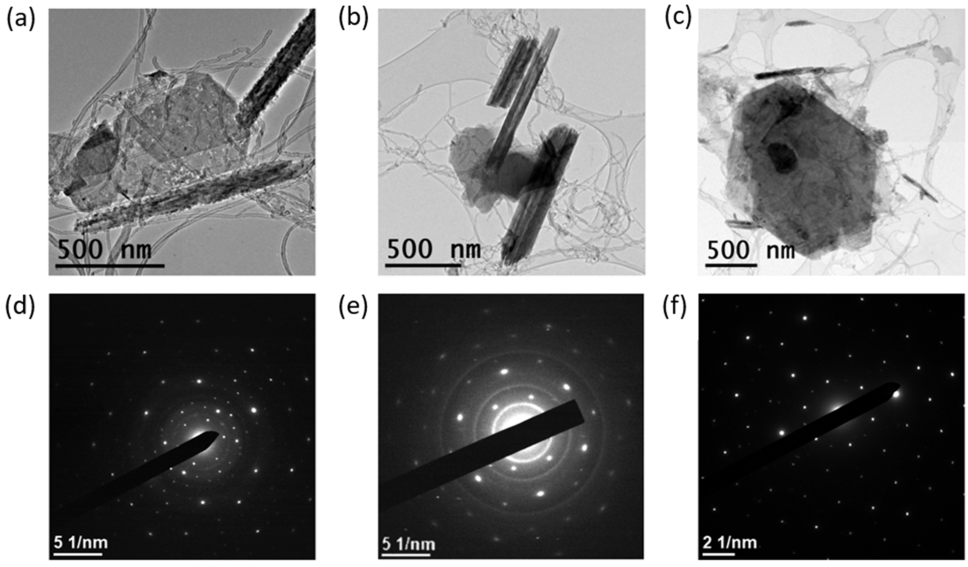

Figure 2. TEM characterization of the α-MnO_2 cathodes discharged in (a, d) $ZnSO_4$ electrolyte, (b, e) $Zn(CF_3SO_3)_2$ electrolyte, and (c, f) $Zn(CH_3COO)_2$ electrolyte showing images of the α-MnO_2 rods and the platelet-shaped materials deposited (a–c) and diffraction patterns of the platelet-shaped materials (d–f).

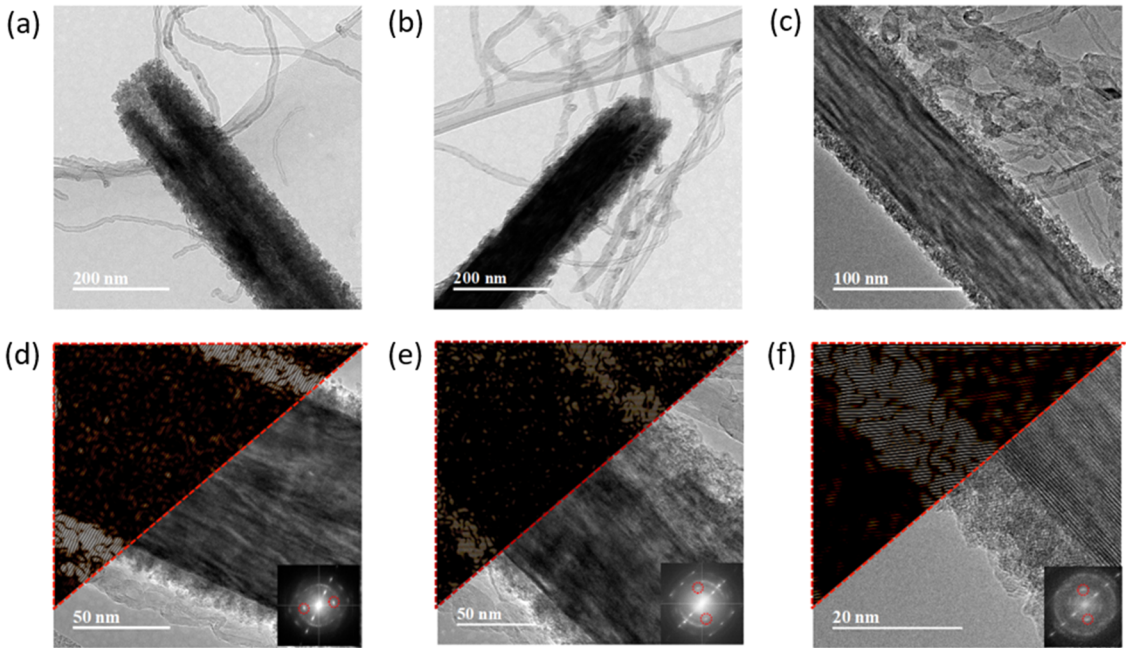

Figure 3. TEM images of the charged α-MnO_2 cathodes in (a) $ZnSO_4$, (b) $Zn(CF_3SO_3)_2$, and (c) $Zn(CH_3COO)_2$ electrolytes after one charge cycle demonstrating the formation of surface deposits during charging. Higher-resolution images with inset power spectra and overlaid with filtered images (outlined in red) using the red, circled areas of the power spectra (d–f) for the $ZnSO_4$, $Zn(CF_3SO_3)_2$, and $Zn(CH_3COO)_2$ cycled sample, respectively. In these filtered areas of the images, brighter sections correspond to areas that generate the highlighted signal in the power spectra.

which corresponds to larger (001) interplanar spacings (10.90 Å for ZHS, 13.52 Å for ZHT and 13.40 Å for ZHA).

In the XRD patterns of the charged cathodes, the ZHS, ZHA, and ZHT peaks disappear, leaving only peaks of the pristine materials (Figure 1b), likely unreacted α-MnO_2. For all three charged cathode patterns, α-MnO_2 peak intensities are lower compared to the pristine pattern, suggesting decreased weight fractions. Additional lab-based XRD scans (Figure S2) were performed to quantify the α-MnO_2 phase fraction after the first discharge and first charge, for which the (002) peak of CNT at ~26° [45] was utilized as an internal standard for XRD weight fraction analysis via peak intensity ratios.[46] The results in Table S1, indicate that ~60% of α-MnO_2 within the cathode remained after the first discharge in the $ZnSO_4$, $Zn(CH_3COO)_2$, and $Zn(CF_3SO_3)_2$ cells and the α-MnO_2 weight fraction did not increase upon charge.

The α-MnO_2 cathodes were examined with TEM after the first discharge (Figure 2) and first charge (Figure 3). Upon the initial discharge, α-MnO_2 nanorods in all three electrolytes show signs of dissolution on the surface and near the end of the rods (Figure 2a–c). Precipitation of a platelet-shaped material was observed alongside the partially dissolved nanorods. The platelet-shaped materials have sixfold symmetry viewed normal to the plate surfaces with diffraction patterns

https://doi.org/10.1021/jacs.2c09477
J. Am. Chem. Soc. 2022, 144, 23405–23420

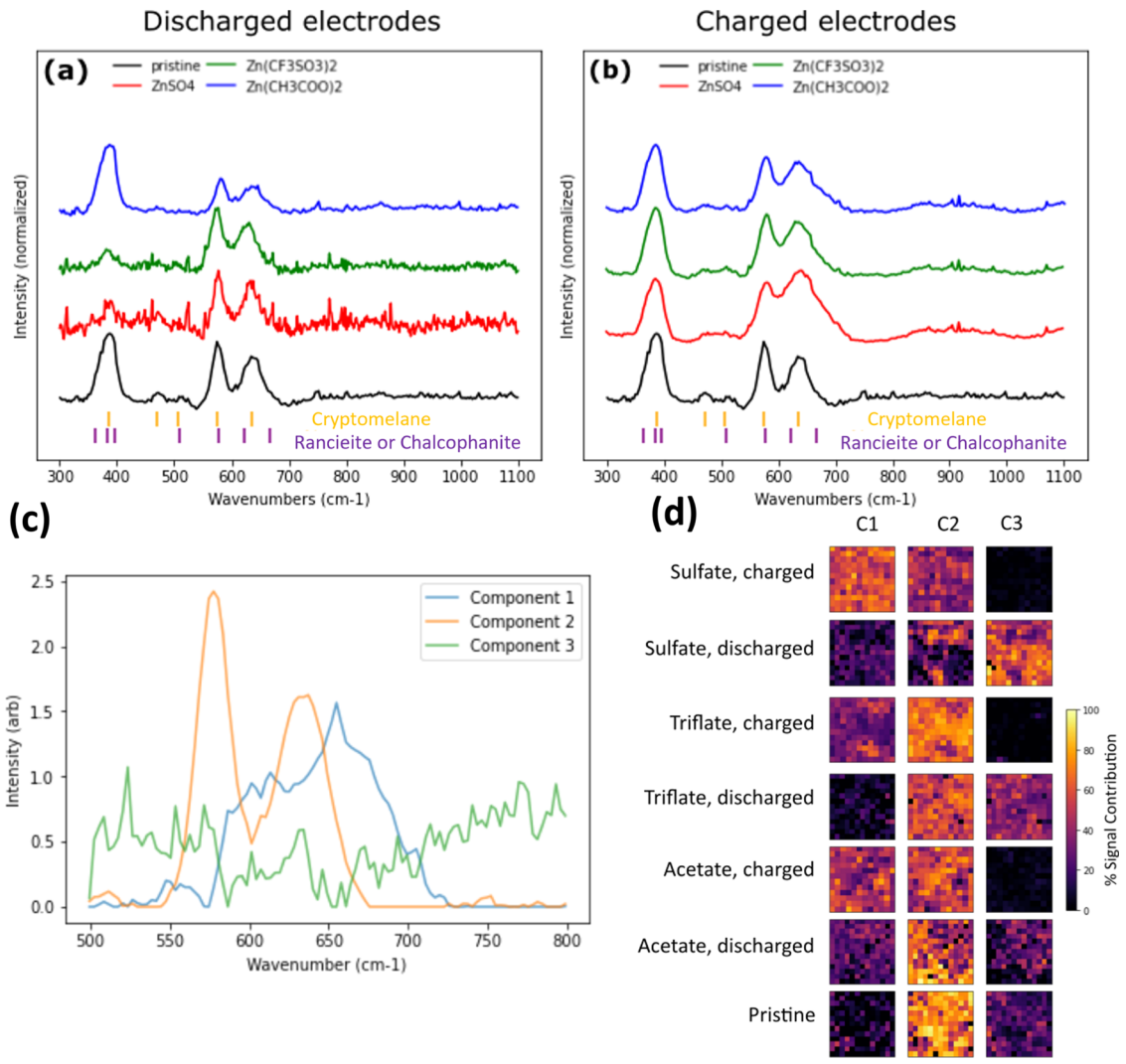

Figure 4. Raman spectra of (a) discharged and (b) charged electrodes. Tick marks along the bottom indicate positions of peaks originating from the cryptomelane tunnel phase (orange) and layer phase (purple). (c) NMF components unmixed from confocal Raman datasets. The extracted pseudospectral signal components were identified, where Component 1 = layered phase, Component 2 = cryptomelane, and Component 3 = residual background. (d) Spatial distribution maps of the identified components on the surface of the *ex situ* electrodes. Component weights were normalized for visualization by their contribution to the total measured signal at a given location.

shown in Figure 2d–f. The diffraction pattern of the discharge product in $ZnSO_4$ electrolyte matches well to the known structure of zinc hydroxy sulfate (ZHS) (Figure 2d), and while no well-established crystal structure of the analogous acetate (ZHA) and triflate salts (ZHT) have been reported, the diffraction pattern symmetry and plate morphology are characteristic of a layered Zn structure consistent with the formation of the zinc hydroxide anion precipitates.

Imaging of the first charged electrodes in $ZnSO_4$, $Zn(CF_3SO_3)_2$, and $Zn(CH_3COO)_2$ electrolytes is shown in Figure 3. The samples from the three electrode types contain rods of α-MnO_2 coated with material deposited on the surface from the electrochemical charge, with the deposited material mostly consisting of a Zn/Mn-containing phase as indicated by EELS mapping (Figure S3). EELS phase maps and spectra of the charged cathodes in Figure S4 also demonstrate that there is a clear distinction between the deposited, surface phase (orange) and the parent α-MnO_2 nanorods (blue), particularly in the O-K edge. The maps in Figure S4 are generated using peak fitting of the O and Mn edges, which have unique profiles for each phase. For cathodes charged in all three electrolytes, measuring the Mn valence via the white line ratios yields values of approximately 4 in the α-MnO_2 nanorods. The surface phase has a reduced valence compared to the bulk, with measured values of approximately 3.4, 3.1, and 3.0 for cathodes charged in $ZnSO_4$, $Zn(CF_3SO_3)_2$, and $Zn(CH_3COO)_2$ electrolytes, respectively. In Figure 3d–f, the red, circled signal in the inset power spectra corresponds to the Zn/Mn phase which is unidentified due to the presence of only one discernable lattice spacing. A spinel $ZnMn_2O_4$ phase is also identified in some areas of the cathode charged in $Zn(CF_3SO_3)_2$ electrolyte (Figure S5), though it was only observed sparsely across the cathode and the overall phase fraction of spinel is very small. This would suggest the spinel phase is only a minor product and its phase fraction is likely below the detection limit of bulk techniques. Major distinctions among the cathodes can be found in the thickness and compositions of the surface layer. The cathodes charged in $ZnSO_4$ and $Zn(CH_3COO)_2$ electrolytes have rather uniform coatings, with a 10–13 nm layer for $ZnSO_4$ and a 9–11 nm layer for $Zn(CH_3COO)_2$. In contrast,

https://doi.org/10.1021/jacs.2c09477
J. Am. Chem. Soc. 2022, 144, 23405–23420

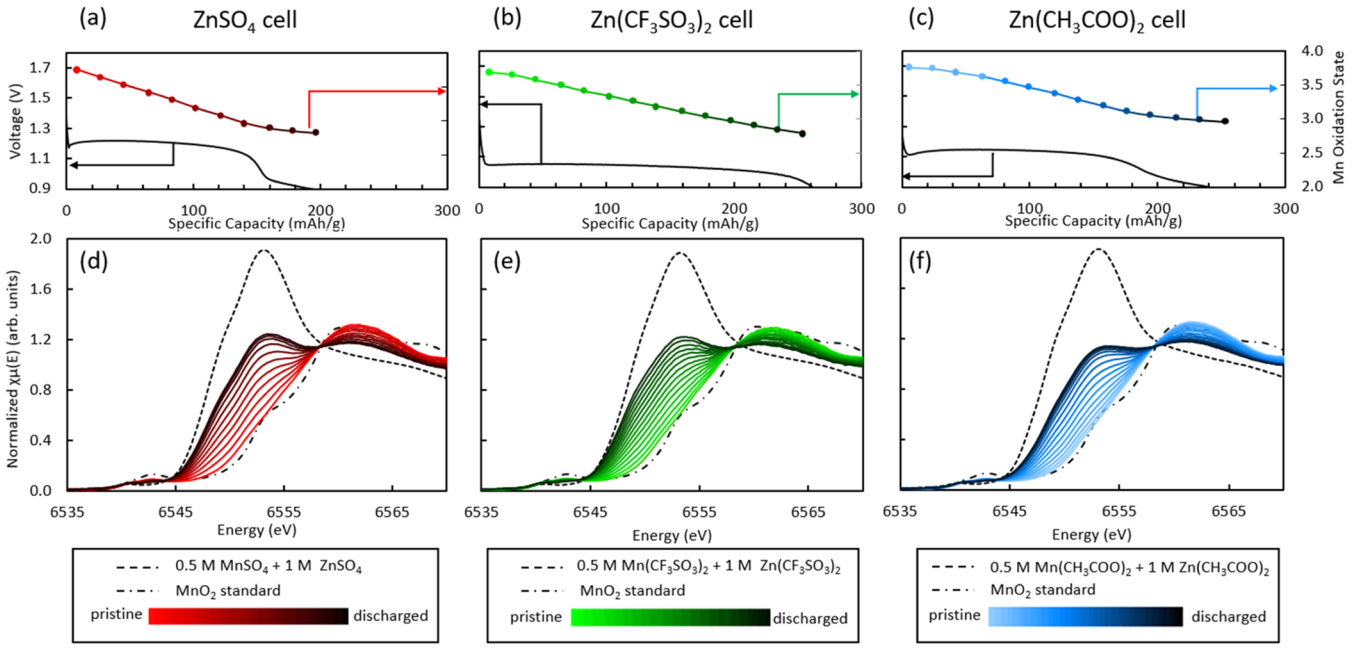

Figure 5. Voltage profile of the *operando* cells during discharge plotted with LCF-calculated average Mn oxidation state for (a) $ZnSO_4$, (b) $Zn(CF_3SO_3)_2$, (c) $Zn(CH_3COO)_2$. *Operando* XANES evolution of the (d) $ZnSO_4$, (e) $Zn(CF_3SO_3)_2$, and (f) $Zn(CH_3COO)_2$ cells.

the $Zn(CF_3SO_3)_2$ cycled cathode has a thicker, more irregular coating ranging from 15 to 21 nm consistent with the relatively higher specific capacity of the $Zn(CF_3SO_3)_2$ cell (Figure S1b).

The surface deposits present in all three electrolyte systems are preferentially aligned on the α-MnO_2 rods, which is demonstrated in the filtered HREM images in Figure 3d–f. The filtered images are generated with red highlighted areas of the inset power spectra, demonstrating that (1) the signal in those areas of the spectra is due to the surface deposits and (2) the surface deposits share a similar crystallographic orientation at the top and bottom faces of the rods as viewed. We note some signal in the middle of the rod in Figure 3e, possibly due to material deposition on the inner surface of the hollow α-MnO_2 rods.

Raman spectroscopy was utilized to identify the less crystalline Zn/Mn-containing products formed under charge in the cycled cathodes. Each spectrum is the average of 169 individual spectra collected at different sites on the sample surface. The average spectrum collected from the pristine electrode exhibits peaks associated with α-MnO_2 only, with bands appearing at 387, 471, 494, 507, 577, and 635 cm^{-1} in agreement with previously published studies.[47] Furthermore, electrodes discharged in $ZnSO_4$, $Zn(CH_3COO)_2$, and $Zn(CF_3SO_3)_2$ electrolytes include Raman spectra that resemble the pristine electrode and the original α-MnO_2 material (Figure 4a), consistent with XRD results, indicating the presence of unreacted residual α-MnO_2 in the discharged electrodes. Upon charge, a new peak emerged around 667 cm^{-1}, suggesting the formation of layered Zn–Mn–O phases (Figure 4b). The detailed Raman band assignments are summarized in Table S5. The Raman spectra were processed using non-negative matrix factorization (NMF) to identify and unmix the relative contributions of each chemical constituent to each measured spectrum. NMF assumes that each spectrum is a purely additive weighted linear sum of a finite number of fundamental components (or *endmembers*) and learns these fundamental components and their associated weights from the variations between individual spectra. To train the rank-3 NMF model, the spectra obtained in the surface maps of the seven measured electrodes were pooled into a single training dataset containing 1096 spectra. Rank-2, rank-4, and rank-5 models were also trained on the same dataset, with the result that the rank-3 model produced the most meaningful and interpretable endmembers; namely, component 1 was associated with the layered charge product, component 2 was identified as the pristine cryptomelane material, and component 3 represents the residual signal baseline (Figure 4c). After comparison with previously published spectra of layered MnO_2 phases,[48] component 1 was found to exhibit a Raman spectrum very similar to that of layered rancieite $(Ca,Mn^{2+})_{0.2}(Mn^{4+},Mn^{3+})O_2{\cdot}0.6H_2O$ or chalcophanite $ZnMn_3^{4+}O_7{\cdot}3H_2O$.

By comparing the normalized signal intensity of the NMF endmember resembling the layer phase (component 1) across the various electrolyte and charge/discharge conditions, it was observed that the layer phase was present in appreciable amounts only in the charged electrodes, suggesting the formation of the layered phase during charge and loss of the same phase during discharge (Figure 4d).[48] Formation of a layered phase during charging of α-MnO_2 electrodes is consistent with previously published studies.[49] Woodruffite $([Zn,Mn^{2+}]Mn_3^{4+}O_7{\cdot}3H_2O)$ has alternatively been proposed as the charge product of an α-MnO_2 electrode;[50] however, we found no evidence of the formation of woodruffite in any electrode, indicated by the absence of a measurable peak at 734 cm^{-1}.[47] NMF analysis of the Raman mapping datasets clearly indicates that the chemical environment at the surface of the charged electrodes is affected by the character of the electrolyte anions. The cell charged in $ZnSO_4$ exhibited the highest percentage of layer phase compared with those in the other two electrolyte systems. In addition, the α-MnO_2 phase was identified in the charged electrodes in all three electrolytes (Figure 4d). The *ex situ* Raman spectroscopy data confirm that there are unreacted pristine α-MnO_2 materials present in both

https://doi.org/10.1021/jacs.2c09477
J. Am. Chem. Soc. 2022, 144, 23405–23420

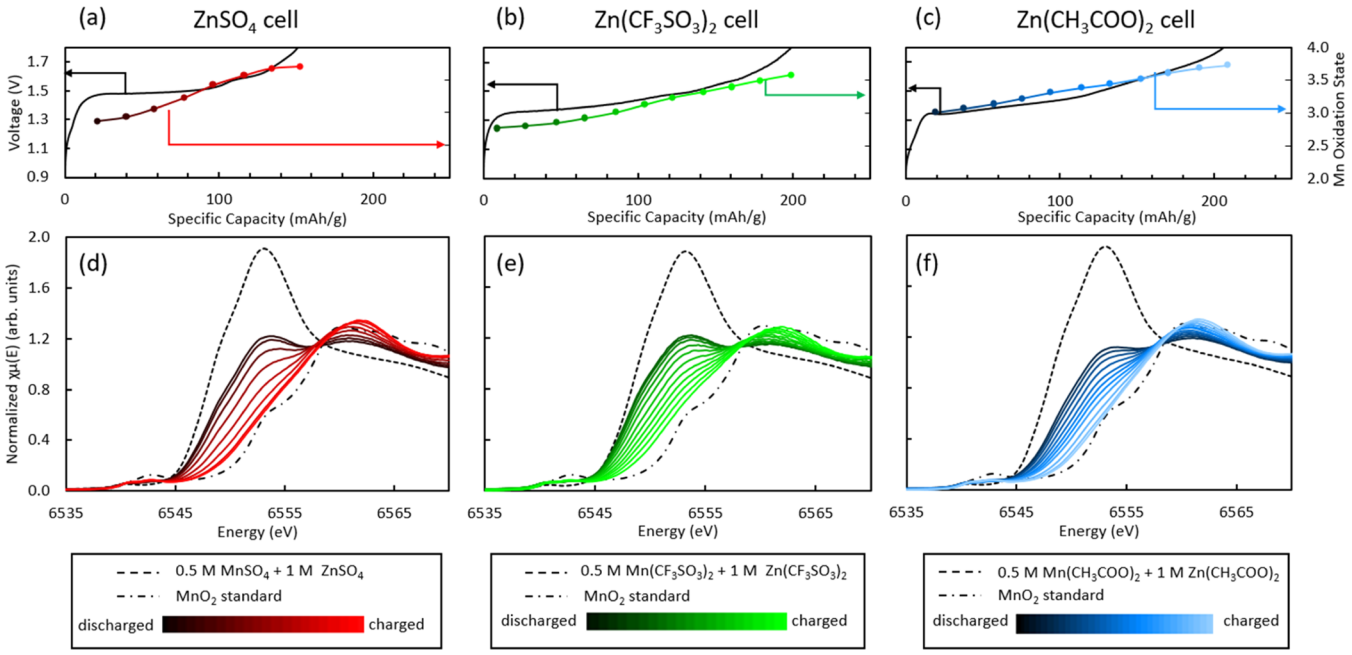

Figure 6. Voltage profile of the *operando* cells during charge plotted with LCF-calculated average Mn oxidation state for (a) $ZnSO_4$, (b) $Zn(CF_3SO_3)_2$, and (c) $Zn(CH_3COO)_2$. *Operando* XANES evolution of the (d) $ZnSO_4$, (e) $Zn(CF_3SO_3)_2$, and (f) $Zn(CH_3COO)_2$ cells.

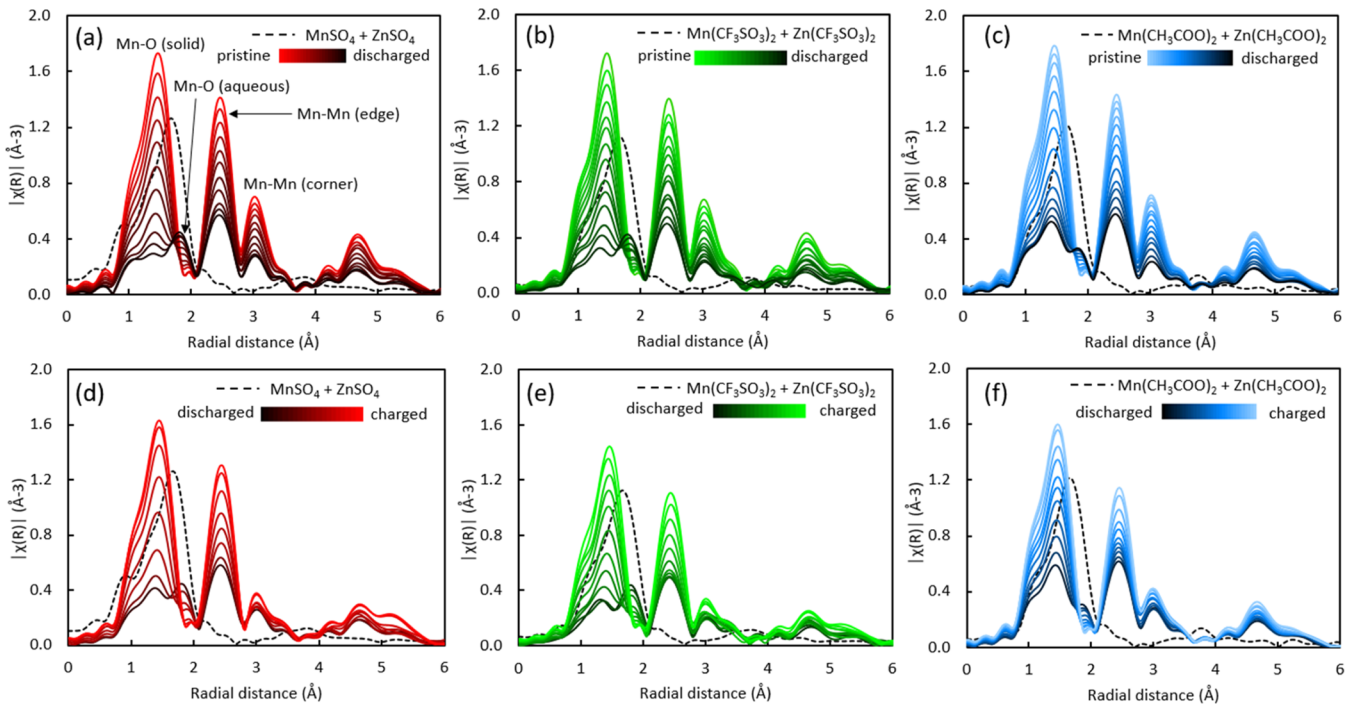

Figure 7. *Operando* EXAFS evolution in *r*-space during discharge for the (a) $ZnSO_4$, (b) $Zn(CF_3SO_3)_2$, and (c) $Zn(CH_3COO)_2$ cells. Corresponding EXAFS evolution during charge for the (d) $ZnSO_4$, (e) $Zn(CF_3SO_3)_2$, and (f) $Zn(CH_3COO)_2$ cells.

discharged and charged electrodes, while the manganese layered phase material only appears in the charge states in the three electrolytes.

Operando XAS Characterization. *Operando* Mn K-edge XAS spectra were measured in transmission geometry during Galvanostatic cycling of the three cells with 1 M $ZnSO_4$, 1 M $Zn(CF_3SO_3)_2$, or 1 M $Zn(CH_3COO)_2$ electrolytes. Due to the measurement geometry relative to the custom cell configuration, the oxidation state and coordination environment evolution of Mn within the cathode and the electrolyte can be effectively followed. Figure 5 presents the *operando* XANES evolution during the initial discharge of the three cell types along with their corresponding voltage profiles. Linear combination fitting (LCF) was performed for each XANES scan to obtain an average Mn oxidation state (OS) within the cells using $KMn_8O_{16(s)}$ values and corresponding aqueous Mn^{2+} standards. During the initial discharge, the progression of the XANES data is similar among all three cells, where the X-ray absorption edge shifts to lower energies. This shift suggests a decrease in the average Mn oxidation state, consistent with

https://doi.org/10.1021/jacs.2c09477
J. Am. Chem. Soc. 2022, 144, 23405−23420

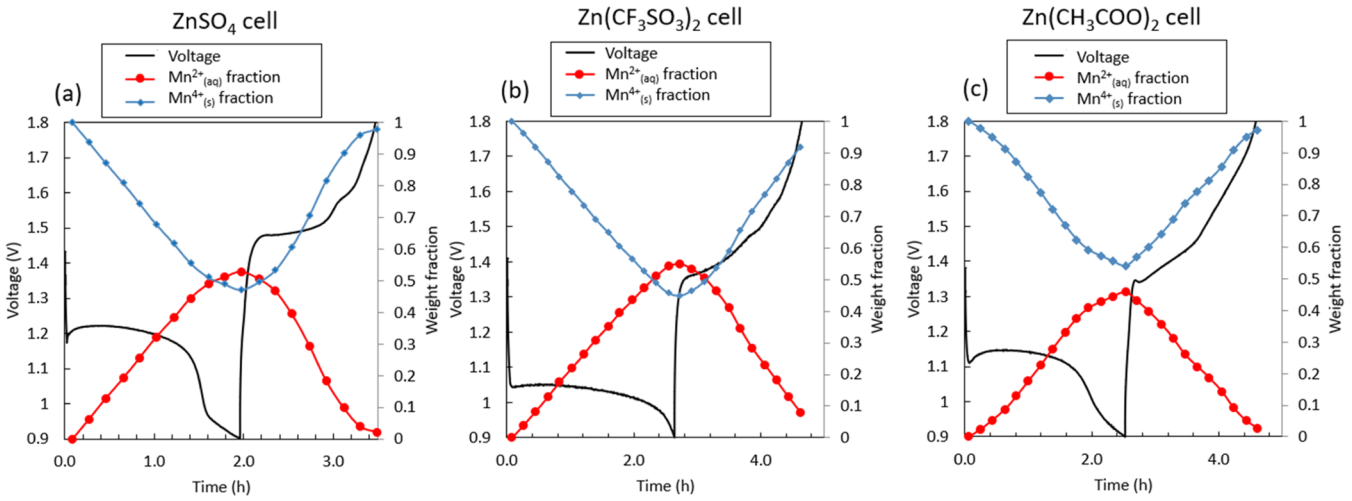

Figure 8. XANES-LCF results showing the aqueous/solid Mn weight fraction of the *operando* cells during the first-cycle (a) $ZnSO_4$, (b) $Zn(CF_3SO_3)_2$, and (c) $Zn(CH_3COO)_2$ cells.

the average Mn oxidation state change determined from LCF (Figure 5a–c). As listed in Table S2, the average Mn oxidation states at the end of the first discharge fitted with the XANES-LCF method were 2.82, 2.78, and 2.96 for the $ZnSO_4$, $Zn(CF_3SO_3)_2$, and $Zn(CH_3COO)_2$ cells, respectively (Figure 5d–f).

The first charge process of the three *operando* cells as well as the progression of the XANES data are plotted in Figure 6. During charge, the absorption edges of the XANES spectra increase, corresponding to the end-of-charge average Mn OS of 3.71, 3.58, and 3.73 for the $ZnSO_4$, $Zn(CF_3SO_3)_2$, and $Zn(CH_3COO)_2$ cells calculated by LCF, respectively (Table S2). Notably, the corresponding average Mn oxidation state values for each cell type upon full charge are slightly lower than the pristine values of 3.73, 3.69, and 3.75 for the $ZnSO_4$, $Zn(CF_3SO_3)_2$, and $Zn(CH_3COO)_2$ cells, respectively. Such oxidation state changes were attributed to the structural and chemical differences between the charge product and the pristine material. As the Raman spectroscopy in the above section indicated that the charge product is a layered zinc manganese oxide, such material typically consists of MnO_x layers with Zn^{2+} ions inserted in between the layers. This type of structure allows the incorporation of a relatively large number of divalent cations like Zn^{2+} into the structure,[51−53] compared to the monovalent K^+-incorporated pristine α-MnO_2. Therefore, the charge product tends to have a lower oxidation state due to the presence of Zn^{2+} compared to the pristine material.

Structural insight can be obtained in the EXAFS region of the collected XAS spectra.[54] As seen in the *k*-space spectra overlay, the coordination environment of the Mn centers changes during discharge and charge for all three cell types (Figure S6). To better elucidate the local structure around Mn centers, the collected *operando* EXAFS spectra were Fourier-transformed into radial space (*r*-space), where the changes in each coordination sphere can be discriminated. Figure 7 shows the *operando* EXAFS evolution of all three cells during the initial discharge and subsequent charge in *r*-space. The *r*-space EXAFS spectra of all three cells have similar major peaks. As shown in Figure 7a, the first major peak at ∼1.5 Å corresponds to the first-shell Mn−O scattering path within the solid MnO_2 structure, the second major peak at ∼2.5 Å corresponds to the second-shell Mn−Mn scattering path, and the third major peak at ∼3.0 Å corresponds to the third-shell Mn−Mn scattering path. Notably, the second-shell Mn−Mn scattering path represents the relative position of two edge-sharing MnO_6 octahedra in the MnO_2 structure, while the third-shell Mn−Mn scattering path represents the relative position of two corner-sharing MnO_6 octahedra characteristic to α-MnO_2.[55−57] The EXAFS spectra of all three cells demonstrate similar progression over the initial discharge, where the overall *r*-space peak intensities gradually decrease, accompanied by the growth of a new peak at ∼1.9 Å. Comparison with aqueous Mn^{2+} EXAFS standard for the three different electrolytes indicates that this peak likely corresponds to the first-shell Mn−O scattering path in solvated $[Mn(H_2O)_6]^{2+}$ ions.[58,59] Upon the first charge, all but the third-shell Mn−Mn peak restores to the pristine intensity, and the aqueous Mn−O peak vanishes for all three cells. The differences in the EXAFS spectra between the fully charged cell and the pristine cell suggest that upon charge, a charge product with a different Mn-centered local structure than the pristine α-MnO_2 has formed.

Overall, both the XANES and EXAFS suggest that Mn^{2+} dissolves during the initial discharge of the *operando* cells with 1 M $ZnSO_4$, 1 M $Zn(CF_3SO_3)_2$, or 1 M $Zn(CH_3COO)_2$ electrolytes, and during the subsequent charge the Mn^{2+} is oxidized and deposits on the cathode. Previously, a reversible Mn dissolution−deposition process was demonstrated using *operando* X-ray fluorescence mapping for aqueous Zn/MnO_2 cells with 2 M $ZnSO_4$ electrolyte[22] and the results can be rationalized through a similar dissolution−deposition process in the electrolyte systems characterized here. Quantitative analysis of EXAFS data was used to confirm the existence of Mn^{2+} in all systems and resolve the structural evolution associated with Mn dissolution−deposition.

XANES Analysis. The Mn dissolution−deposition process involves dissolved solvated aqueous Mn^{2+} ions and solid MnO_x. The XAS spectra of a mixture of different Mn-containing components are in principle the summation of the XAS spectra of each component.[60] Thus, LCF of *operando* XAS data in the XANES region was performed using aqueous Mn^{2+} standards (1 M $ZnSO_4$ + 0.5 M $MnSO_4$, 1 M $Zn(CF_3SO_3)_2$ + 0.5 M $Mn(CF_3SO_3)_2$, or 1 M $Zn(CH_3COO)_2$

https://doi.org/10.1021/jacs.2c09477
J. Am. Chem. Soc. 2022, 144, 23405−23420

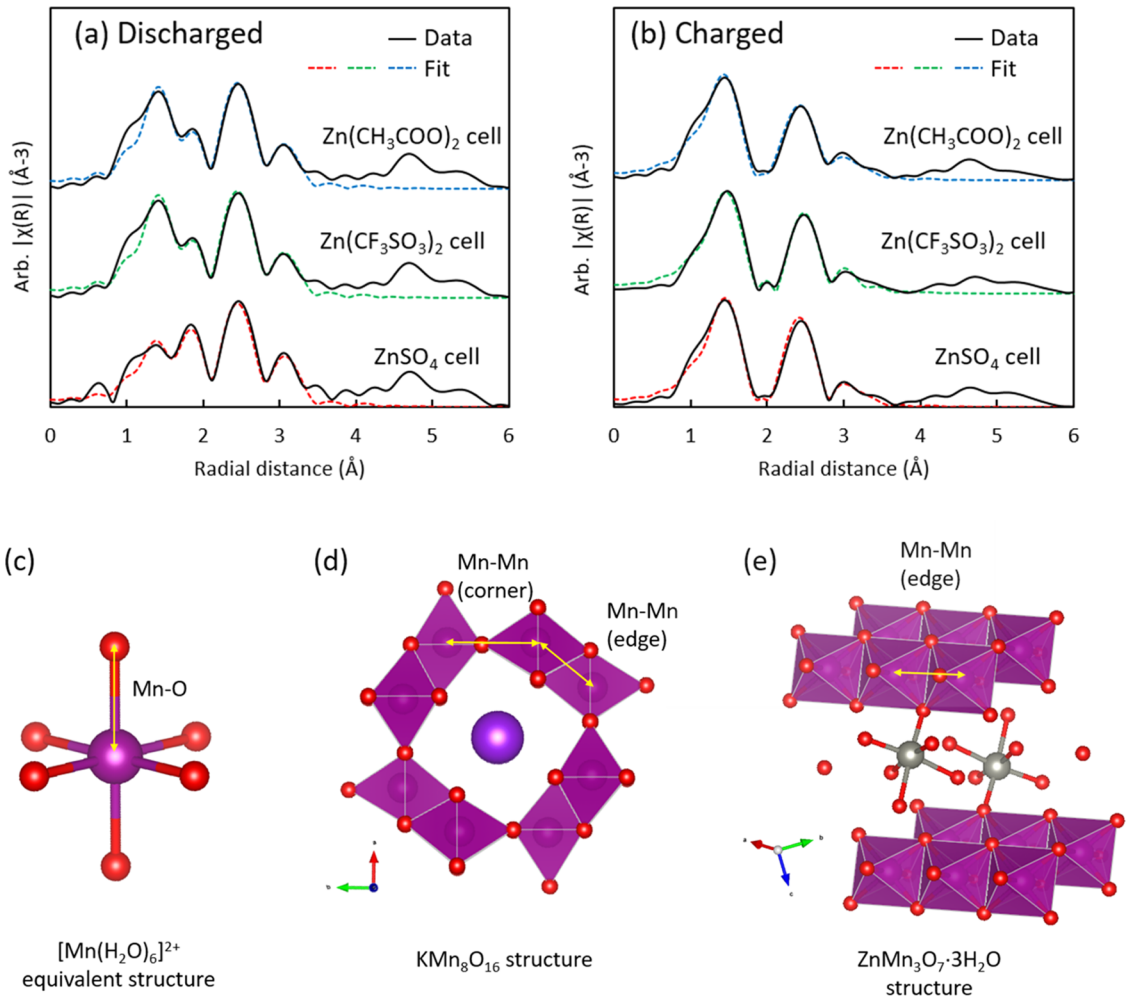

Figure 9. EXAFS fitting results of (a) fully discharged *operando* cell scans and (b) fully charged *operando* cell scans. (c–e) Theoretical structures used to perform FEFF calculations during EXAFS fitting.

+ 0.5 M $Mn(CH_3COO)_2$) and pristine scans of the corresponding *operando* cell to obtain aqueous and solid Mn weight fractions within the cells during the electrochemical reduction and oxidation (Figure 8).

For the XAS spectra collected during the initial discharge process of the three cell types, LCF-fitted weight fractions of solid/aqueous Mn demonstrate Mn dissolution associated with the electrochemical process (Figure 8). By the end of the initial discharge, ~50% of Mn has dissolved from the cathode to form Mn^{2+}. During charge, LCF results suggest that while the majority of the dissolved Mn^{2+} has redeposited as a solid, a small amount seemed to remain unoxidized as the solid fraction did not return to 1 at the end of charge for all three cells. This is expected as it is reported that Mn^{2+} oxidation–deposition in a mildly acidic aqueous environment might stop before all available Mn^{2+} can be oxidized, where a minimum Mn^{2+} concentration must be maintained for the deposition process to occur.[61] Thus, our observation of a small amount (~0.1 weight fraction) of retained Mn^{2+} after charge via XANES-LCF here is consistent with prior reports. The solid/aqueous Mn weight fraction progression over the first full cycle for all three cells shows increases and decreases coincident with the electrochemistry.

Multiphase EXAFS Fitting. EXAFS fitting was used to resolve the Mn-containing products using theoretical FEFF-calculated structures. FEFF-based EXAFS fitting with theoretical structures is commonly performed on a material with a single phase of the absorbing element. When different phases of the absorbing element are present, multiple FEFF calculations using different theoretical structures can be included in the fit with a "mixing factor" to properly approximate experimental data of these mixtures, as demonstrated previously.[62] The EXAFS spectrum of a multiphase material is the summation of its individual components expressed as[60]

$$\chi(k) = \sum_i w_i \chi_i(k) \tag{1}$$

where w_i is the weight fraction of component i and $\chi_i(k)$ is the mathematical expression established for EXAFS spectra of a single component i

$$\chi_i(k) = \sum_j \frac{S_{0,i}^2 N_j e^{-2k^2\sigma_j^2} e^{-2R_j/\lambda(k)} f_j(k)}{kR_j^2} \sin[2kR_j^2 + \delta_j(k)] \tag{2}$$

The above equation is the EXAFS equation and is utilized by FEFF6 to calculate theoretical EXAFS patterns. The variables related to amplitude and intensity of the EXAFS spectra are S_0^2 (amplitude reduction factor) and N_j (coordination number),

https://doi.org/10.1021/jacs.2c09477
J. Am. Chem. Soc. 2022, 144, 23405–23420

Table 2. EXAFS Fitting Results of Fully Discharged *Operando* Cells[a]

sample	theoretical FEFF	phase fraction	shell	scattering path	S_0^2	N	ΔE_0 (eV)	R (Å)	σ^2	R-factor
$ZnSO_4$ cell at full discharge	$[MnO_6]$	0.54(0.013)	1st	Mn−O (aqueous)	**0.68**	**6**	−2.53	2.17(0.013)	0.0083	0.017
	cryptomelane ($K_{1.33}Mn_8O_{16}$)	0.46(0.013)	1st	Mn−O (solid)	**0.83**	**6**	9.67	1.88(0.0072)	0.0037	
			2nd	Mn−Mn (edge)		**4**		2.86(0.0096)	0.0033	
			3rd	Mn−Mn (corner)		**4**		3.44(0.015)	0.0049	
$Zn(CF_3SO_3)_2$ cell at full discharge	$[MnO_6]$	0.59(0.01)	1st	Mn−O (aqueous)	**0.80**	**6**	−4.28	2.15(0.012)	0.0094	0.014
	cryptomelane ($K_{1.33}Mn_8O_{16}$)	0.41(0.01)	1st	Mn−O (solid)	**0.63**	**6**	8.87	1.88(0.0060)	0.0015	
			2nd	Mn−Mn (edge)		**4**		2.86(0.0086)	0.0024	
			3rd	Mn−Mn (corner)		**4**		3.44(0.013)	0.0042	
$Zn(CH_3COO)_2$ cell at full discharge	$[MnO_6]$	0.55(0.01)	1st	Mn−O (aqueous)	**0.82**	**6**	−4.50	2.15(0.022)	0.013	0.018
	cryptomelane ($K_{1.33}Mn_8O_{16}$)	0.45(0.01)	1st	Mn−O (solid)	**0.70**	**6**	8.34	1.88(0.0071)	0.0018	
			2nd	Mn−Mn (edge)		**4**		2.85(0.0098)	0.0028	
			3rd	Mn−Mn (corner)		**4**		3.43(0.016)	0.0057	

[a] S_0^2: amplitude reduction factor; N: coordination number; ΔE_0: shift in edge energy; R(Å): atomic distance; σ^2: Debye−Waller factor. The bold numbers were obtained by LCF (weight fraction), reference EXAFS fitting (S_0^2), or ideal values based on stoichiometry (N), and were fixed during these fitting operations.

where j denotes each scattering path within a FEFF calculation. To incorporate multiple phases, the EXAFS equation can be written by combining eqs 1 and 2

$$\chi(k) = \sum_i w_i \sum_j S_{0,j}^2 N_j F_j(k) = \sum_i \sum_j w_i S_{0,j}^2 N_j F_j(k) \quad (3)$$

where $F(k)$ represents the remaining terms in eq 2 as a function of k. Equation 3 shows that w_i, S_0^2, and N_j will directly affect the EXAFS amplitude in k-space and the peak intensities in r-space. Hereby, we propose a multiphase EXAFS fitting model based on solid and aqueous components to deconvolute the multiphase discharge and charge reactions in the Zn/MnO_2 systems with different mildly acidic electrolytes, for which the EXAFS equation in k-space can be written as

$$\chi(k) = w_{aq} S_{0,aq}^2 N_{aq} F_{aq}(k) + w_s S_{0,s}^2 N_s F_s(k) \quad (4)$$

where subscript aq denotes aqueous component and subscript s denotes solid component.

In Figure 7, the significant peak intensity change observed in the *operando* r-space EXAFS pattern is ascribed to changes in the aqueous/solid Mn weight fraction as the amplitude reduction factor and coordination number have physical constraints[60] and do not vary significantly under the experimental conditions employed in this work. Several theoretical structures were used to perform the FEFF calculations, including $K_{1.33}Mn_8O_{16}$ cryptomelane[63] (KMO), $ZnMn_3O_7{\cdot}3H_2O$ chalcophanite[64] (ZMO), and $[MnO_6]$ (Figure 9c−e). KMO represents the pristine α-MnO_2 material within the cathode. ZMO represents the layered Zn−Mn oxide structure identified by Raman spectroscopy (Figure 4).

The additional theoretical structure, $[MnO_6]$, is the equivalent structure of solvated $[Mn(H_2O)_6]^{2+}$ ions in water for EXAFS analysis.[58,59,65] EXAFS studies on inorganic Mn salts dissolved in water showed that for Mn^{2+} concentrations between 0.05 and 6 M, Fourier-transformed EXAFS data generally produces one major peak at ∼1.7 Å,[58,59] which was verified in this work with a series of Mn^{2+} EXAFS standards with Mn^{2+} concentrations between 0.2 M and 1.0 M (Figure S7). Note that the peak position in the EXAFS r-space does not correspond to the actual atomic distance, a constant phase shift (in this case about 0.5 Å) is always present in the EXAFS model as δ_j in eq 2. The results for the standards agree with the literature as the r-space amplitude is independent of absorbing ion concentration. The results of EXAFS fitting of solvated $[Mn(H_2O)_6]^{2+}$ ions performed with $[MnO_6]$ in previous work[58,59,65] show that within the EXAFS region, the $[Mn(H_2O)_6]^{2+}$ structure can be well represented by a $[MnO_6]$ theoretical structure (Figure 9c) with a slightly larger Mn−O distance than typical $[MnO_6]$ in solid manganese oxides (Table S3). This EXAFS result indicates that when Mn^{2+} dissolves in water, the Mn^{2+} center can be represented as $[Mn(H_2O)_6]^{2+}$. Notably, when aqueous Mn^{2+} and Zn^{2+} are both present, the increase in pH might also trigger the precipitation of $Mn(OH)_2$ or related structures, meaning that Mn^{2+} might not be the only Mn-containing discharge product. Therefore, we compared the *ex situ* XRD patterns of the discharged cathodes to $Mn(OH)_2$ reference,[66] as seen in Figure S13. As the major peaks from the $Mn(OH)_2$ reference do not match our diffraction pattern well, it is unlikely to be a major discharge product.

One previous study hypothesized that Mn^{2+} might precipitate in the form of Mn-containing ZHS in $ZnSO_4$ electrolyte, where Mn^{2+} substitutes some of the Zn^{2+} sites in the ZHS layers.[67] However, such precipitation could not be detected by XRD as the Mn-ZHS has the same crystal structure as regular ZHS. To further explore this possibility here, we examined the crystal structures of ZHS and $Mn(OH)_2$, as shown in Figure S14. The local structures of ZHS and $Mn(OH)_2$ are indeed highly similar with very close second-shell metal−metal distances, which means that Mn^{2+} substitution of Zn^{2+} sites might be possible. In the Mn-substituted ZHS structure, the second-shell near neighbor around substituted Mn centers would be a Zn atom that is

https://doi.org/10.1021/jacs.2c09477
J. Am. Chem. Soc. 2022, 144, 23405−23420

Table 3. EXAFS Fitting Results of Fully Charged *Operando* Cells[a]

sample	theoretical FEFF	weight fraction	shell	scattering path	S_0^2	N	ΔE_0 (eV)	R (Å)	σ^2	R-factor
$ZnSO_4$ cell at full charge	$[MnO_6]$	0.005(0.063)	1st	Mn−O	**0.83**	**6**	**−4**	**2.18**	0.014	0.0087
	cryptomelane ($K_{1.33}Mn_8O_{16}$)	**0.46**	1st	Mn−O	**0.68**	**6**	8.47	1.86(0.026)	0.0017	
			2nd	Mn−Mn (edge)		**4**		2.92(0.013)		
			3rd	Mn−Mn (corner)		**4**		3.46(0.012)		
	chalcophanite ($ZnMn_3O_7{\cdot}3H_2O$)	0.54(0.063)	1st	Mn−O	**0.68**	**6**	−6.28	1.90(0.031)	0.0048	
			2nd	Mn−Mn (edge)		**4**		2.83(0.0097)		
			3rd	Mn−O		**6**		3.49(0.053)		
$Zn(CF_3SO_3)_2$ cell at full charge	$[MnO_6]$	0.010(0.028)	1st	Mn−O	**0.80**	**6**	**−4**	**2.18**	0.021	0.0080
	cryptomelane ($K_{1.33}Mn_8O_{16}$)	**0.41**	1st	Mn−O	**0.63**	**6**	9.92	1.90(0.014)	0.0014	
			2nd	Mn−Mn (edge)		**4**		2.92(0.0094)		
			3rd	Mn−Mn (corner)		**4**		3.46(0.011)		
	chalcophanite ($ZnMn_3O_7{\cdot}3H_2O$)	0.49(0.028)	1st	Mn−O	**0.63**	**6**	−6.34	1.86(0.015)	0.0035	
			2nd	Mn−Mn (edge)		**4**		2.83(0.0061)		
			3rd	Mn−O		**6**		3.46(0.042)		
$Zn(CH_3COO)_2$ cell at full charge	$[MnO_6]$	0.06(0.030)	1st	Mn−O	**0.82**	**6**	**−4**	**2.18**	0.014	0.011
	cryptomelane ($K_{1.33}Mn_8O_{16}$)	**0.45**	1sr	Mn−O	**0.70**	**6**	9.74	1.91(0.013)	0.0018	
			2nd	Mn−Mn (edge)		**4**		2.92(0.010)		
			3rd	Mn−Mn (corner)		**4**		3.46(0.012)		
	chalcophanite ($ZnMn_3O_7{\cdot}3H_2O$)	0.49(0.030)	1st	Mn−O	**0.70**	**6**	−7.31	1.85(0.015)	0.0042	
			2nd	Mn−Mn (edge)		**4**		2.82(0.0073)		
			3rd	Mn−O		**6**		3.43(0.051)		

[a] S_0^2: amplitude reduction factor; N: coordination number; ΔE_0: shift in edge energy; R(Å): atomic distance; σ^2: Debye−Waller factor. All bold numbers were fixed during fitting, where S_0^2 was obtained from standard EXAFS fitting and N was assumed to be ideal.

~3.4 Å away from the Mn center, meaning that if such structure exists in a sufficient quantity, an intense peak would be observed in the EXAFS r-space pattern at ~3.0 Å. However, the quantitative EXAFS fitting (see Table 2) demonstrates that the peak at ~3.0 Å can be fully accounted for by the undissolved α-MnO_2 in this study, indicating that any other material that generates signal at this distance would not be a major component. Our previous *operando* X-ray fluorescence mapping study of aqueous Zn/α-MnO_2 battery with $ZnSO_4$ electrolyte also demonstrates that the majority of Mn^{2+} generated during discharge will go directly into the electrolyte rather than being precipitated in the cathode.[22] Therefore, it is reasonable to include only $[MnO_6]$ reference structure to represent $[Mn(H_2O)_6]^{2+}$ in this EXAFS fitting analysis.

The EXAFS fitting of the XAS scans on *operando* cells before cycling and XAS scans collected on dissolved 1 M $ZnSO_4$ + 0.5 M $MnSO_4$, 1 M $Zn(CF_3SO_3)_2$ + 0.5 M $Mn(CF_3SO_3)_2$, or 1 M $Zn(CH_3COO)_2$ + 0.5 M $Mn(CH_3COO)_2$ standards was performed first to obtain corresponding amplitude reduction factors for solid Mn components and aqueous Mn components, respectively. The fitting results are shown in Table S4 and Figure S8. These results also show that the KMO reference and the $[Mn(H_2O)_6]^{2+}$ represent the corresponding pristine material and dissolved Mn^{2+} well.

A series of multiphase EXAFS fitting methods were explored to determine the best EXAFS fitting strategy. The final multiphase EXAFS fitting procedure for the *operando* cells used the following constraints: (1) The Mn−O (aq) bond distance was fixed at 2.18 Å to represent $[Mn(H_2O)_6]^{2+}$. (2) The ZMO theoretical structure was included in the fit in addition to KMO and $[MnO_6]$ during the charging process. (3) The KMO weight fraction was assumed to remain unchanged during the charging process, consistent with our quantitative XRD analysis results (Table S1).

The fully discharged scans of each *operando* cell were fit with the $[Mn(H_2O)_6]^{2+}$ reference to account for dissolved Mn^{2+}, and KMO reference to account for undissolved pristine α-MnO_2. The EXAFS fitting results of the fully discharged *operando* cells are shown in Table 2, with corresponding r-space plots shown in Figure 9a. As shown in eq 3, with the phase fraction undetermined, coordination numbers cannot be independently fitted therefore were assumed to be ideal. The results demonstrate that the significant r-space evolution that occurred during discharge can be accounted for by the coexistence of aqueous Mn^{2+} and the pristine α-MnO_2 phase. The fitting results indicate that at full discharge, the r-space spectra of all cells are composed of one major peak from the Mn^{2+} (~1.9 Å) and three major peaks from α-MnO_2 (~1.5, ~2.5, ~3.0 Å). Although an apparent shift of the Mn^{2+} peak is visible throughout the cycling process, it is unlikely caused by the actual change in Mn−O atomic distances. Previous study on dissolved $MnBr_2$ has shown that when aqueous Mn^{2+} EXAFS data were collected without the interference of solid Mn phases, Mn−O atomic distances in $[Mn(H_2O)_6]^{2+}$ do not vary by Mn concentration.[59] We also collected aqueous Mn^{2+} standards of each of the three anions over a concentration range of 0.2 to ~1.0 M, showing that first-shell aqueous Mn−O atomic distances do not vary with Mn concentration (Figure

https://doi.org/10.1021/jacs.2c09477
J. Am. Chem. Soc. 2022, 144, 23405−23420

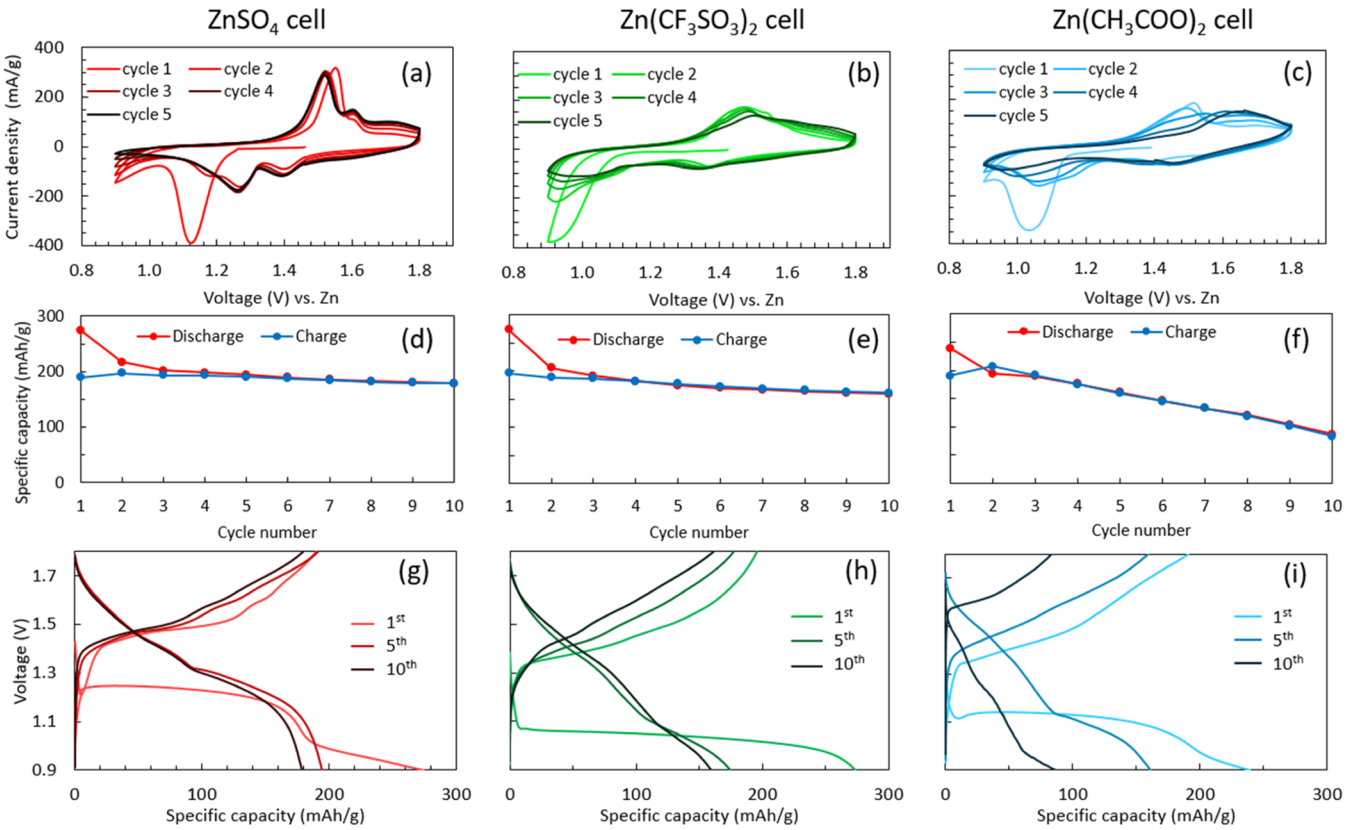

Figure 10. (a–c) Five-cycle CV results and (d–f) 10-cycle capacity retention. (g, h) Voltage profile evolution over the 10 cycles for $ZnSO_4$, $Zn(CF_3SO_3)_2$, and $Zn(CH_3COO)_2$ cells.

S7). Fitting results in Table 2 show KMO and Mn^{2+} phase fractions that are consistent with LCF, predicting over 50% Mn dissolution upon discharge of all cells, demonstrating that the local structures of both phases in all cells remained near ideal compared to reference fitting results (Table S4) with little atomic distance changes. This indicates that upon the initial discharge, pristine α-MnO_2 dissolves in $ZnSO_4$, $Zn(CF_3SO_3)_2$, or $Zn(CH_3COO)_2$ electrolytes to form hydrated $[Mn(H_2O)_6]^{2+}$ ions and the undissolved α-MnO_2 does not change its local structure.

For the EXAFS spectra of fully charged *operando* cells, the Mn^{2+} peak that emerged upon discharge went away, leaving only three major peaks across the first three shells. Those spectra resemble pristine scans (Figure 7) except that the third shell Mn–Mn peaks have visibly diminished. This suggests for Mn in the fully charged cathodes, the number of corner-sharing $[MnO_6]$ octahedra has been significantly reduced. For α-MnO_2 cathodes in lithium-ion batteries, a similar observation was attributed to *in situ* crystallographic transformation caused by lithiation, where the 2×2 tunnel of α-MnO_2 collapses.[57,68] Apparently, this does not apply to the *operando* cells here, as we have demonstrated that pristine α-MnO_2 either dissolved or transformed to a layered Zn–Mn oxide upon initial discharge and the unreacted material did not experience structural change. Here, the Raman spectroscopy characterization in the above section and our previous *ex situ* TEM work showed that a layered zinc manganese oxide occurred in α-MnO_2 cathodes charged in the same group of nonalkaline electrolytes; therefore, the similarly layered ZMO was introduced as a reference for the EXAFS fitting of *operando* cells at full charge. Based on LCF results above, refined EXAFS fitting of the *operando* cells upon full charge was performed with KMO phase fractions constrained to that obtained in Table 2, Figures S9 and S10. Refined EXAFS fitting results shown in Figure 9b, Table 3, and Figures S9 and S10 indicate that upon charge, most Mn^{2+} will convert to solid ZMO, while the unreacted KMO does not experience structural change during the charging process in all cells. The quantitative analysis of the *operando* XAS data has provided bulk-level Mn speciation information on the cell composition progression for aqueous Zn/MnO_2 batteries with 1 M $ZnSO_4$, 1 M $Zn(CF_3SO_3)_2$, or 1 M $Zn(CH_3COO)_2$ electrolytes over the first full cycle. In particular, the Mn redox reaction within all cells could be described by LCF in the XANES region and multiphase EXAFS fitting.

With charge product identified as layered zinc manganese oxide, the faradaic reactions for aqueous Zn/MnO_2 battery cathodes in the presence of 1 M $ZnSO_4$, 1 M $Zn(CF_3SO_3)_2$, or 1 M $Zn(CH_3COO)_2$ electrolytes are proposed. Evidence from the *operando* XAS analysis suggests that for these three electrolyte systems, Mn dissolution–deposition, formation of Zn/Mn oxide, and precipitation of zinc hydroxide species occur in a similar manner during discharge and charge. Upon initial discharge, pristine α-MnO_2 cathode dissolves to form aqueous Mn^{2+}. The precipitation of the zinc hydroxide salts (ZHS, ZHA, and ZHT) is a pH-modulated process[7] that is closely coupled with faradic Mn dissolution,[22,23] which can be described as

https://doi.org/10.1021/jacs.2c09477
J. Am. Chem. Soc. 2022, 144, 23405–23420

$$KMn_8O_{16} + (16 + x)H_2O + \frac{64}{3}Zn^{2+} + \frac{16}{3}SO_4^{2-} + 15e^- \rightarrow 8Mn^{2+} + K^+ + \frac{16}{3}Zn_4(OH)_6SO_4 \cdot xH_2O \quad (5)$$

$$KMn_8O_{16} + (16 + x)H_2O + 20Zn^{2+} + 8CF_3SO_3^- + 15e^- \rightarrow 8Mn^{2+} + K^+ + 4Zn_5(OH)_8(CF_3SO_3)_2 \cdot xH_2O \quad (6)$$

$$KMn_8O_{16} + (16 + x)H_2O + 20Zn^{2+} + 8CH_3COO^- + 15e^- \rightarrow 8Mn^{2+} + K^+ + 4Zn_5(OH)_8(CH_3COO)_2 \cdot xH_2O \quad (7)$$

Thus, the dissolution of pristine α-MnO_2 (KMn_8O_{16}) consumes proton supplied by H_2O molecules in the electrolyte, causing the local pH around the cathode area to increase, then lead to the precipitation of ZHS, ZHT, or ZHA. Upon charge, deposition leads to the formation of layered Zn/Mn oxide accompanied by the dissolution of the zinc hydroxide salts.

Although the initial discharge of all three cells started with a flat voltage plateau, their voltages are different, with the $ZnSO_4$ cell demonstrating the highest voltage (Figure S1b). To further demonstrate the differences in electrochemistry among the three electrolyte systems, CV (Figure 10a−c) and extended cycling (Figure 10d−i) were tested for all three systems. The difference in the discharge plateau is very likely due to the anion effect. Previous work has shown through quantum chemistry calculations that $CF_3SO_3^-$ anion has much higher electrostatic potential and therefore lower molecular polarity index (MPI) (4.68 eV) compared to SO_4^{2-} anions (MPI = 10.47 eV),[69] which results in higher hydrophobicity of $CF_3SO_3^-$ anions. In addition, the electrostatic potential of CH_3COO^- anion lies between $CF_3SO_3^-$ and SO_4^{2-}.[70] As a result, SO_4^{2-} anion tends to bond with H_2O, creating a H_2O-rich environment near the cathode surface while $CF_3SO_3^-$ and CH_3COO^- anion tend to adsorb to the cathode and create a H_2O-poor environment as also demonstrated by molecular dynamics simulation on SO_4^{2-} and $CF_3SO_3^-$ in the previous work.[69] Such H_2O depopulation creates a kinetic barrier for the protonation process needed for Mn dissolution to occur,[71] lowering the discharge voltage plateau. Correspondingly during the charging process, the bulky anion in either $CF_3SO_3^-$ or CH_3COO^- cells will decrease the number of H_2O water molecules surrounding Mn^{2+} ion, mitigating the solvation effect and therefore enhancing charge and ion transfer, lowering the charge voltage plateau.[15] For subsequent cycles, the voltage profiles of all three systems evolve, consistent with a difference between the deposited charge product and the pristine α-MnO_2. Notably for the $Zn(CH_3COO)_2$ cell, a more severe capacity fade was observed over 10 cycles. This might be due to the strong binding between CH_3COO^- and Zn^{2+} ions, which results in slow extraction of CH_3COO^- from ZHA upon charge, therefore limiting Mn^{2+} insertion into ZHA and eventually inhibiting Mn deposition.[23] XRD was collected for 10-cycle charged cathodes from all three electrolyte systems as shown in Figure S12, where peaks from undissolved pristine material are visible in all. To further explore the cause of the voltage plateau differences, Zn−Zn symmetric cells with 1 M $ZnSO_4$, $Zn(CF_3SO_3)_2$, or $Zn(CH_3COO)_2$ electrolyte were assembled and cycled, and the voltage profiles are plotted in Figure S11. It can be seen that the $ZnSO_4$ cell has the smallest overpotential for both Zn stripping and plating followed by $Zn(CH_3COO)_2$ electrolyte and the $Zn(CF_3SO_3)_2$ electrolyte has the highest overpotential for Zn stripping and plating. During the discharge process with Mn dissolution at the cathode and Zn stripping at the anode, a smaller Zn stripping overpotential results in a higher voltage plateau. Thus, the Zn anode interaction with the electrolytes also likely contributes to the voltage profile differences observed during initial discharge for the three electrolyte systems. Furthermore, the measured viscosities of the three electrolytes at room temperature (Table 1) suggest that the viscosity might also have an impact on the first discharge voltage plateau. A higher viscosity is often correlated with the lower ionic diffusion coefficient of an electrolyte.[72] In this case, the first discharge plateau of the three cells can be ranked as $ZnSO_4$ > $Zn(CH_3COO)_2$ > $Zn(CF_3SO_3)_2$, consistent with the room-temperature viscosity of the three electrolytes ranked as $Zn(CF_3SO_3)_2$ > $Zn(CH_3COO)_2$ > $ZnSO_4$.

CONCLUSIONS

An *operando* Mn K-edge XAS technique was used to experimentally probe the α-MnO_2 dissolution−deposition redox process for aqueous zinc batteries with $ZnSO_4$, $Zn(CF_3SO_3)_2$, or $Zn(CH_3COO)_2$ aqueous electrolytes. The *operando* XAS studies were augmented by *ex situ* XRD, TEM, and Raman spectroscopy of the cathode materials. Raman spectroscopy identified less crystalline Mn-containing products formed under charge at the cathodes. Transmission electron microscopy (TEM) provided insight into the morphology and surface condition of the deposited solids. Analysis of the EXAFS data was conducted using a multiphase approach including both solid state and dissolved transition-metal constituents. The results showed that Mn dissolution−deposition process resulted in similar coordination environments, but different distributions of manganese amounts within the solid and in solution for the three mildly acidic electrolytes. The *operando* XAS characterization method offered insights complementary and superior to independent investigations of the solid phases or electrolytes as both the solid and dissolved forms of manganese could be characterized under the same conditions. The methodology provides a useful approach for the bulk characterization of poorly or noncrystalline, multiphase materials, including other polymorphs of Mn_xO_y, in complex environments where the insights are of fundamental importance for further understanding of aqueous electrolyte systems aimed toward large-scale energy storage.

ASSOCIATED CONTENT

Supporting Information

The Supporting Information is available free of charge at https://pubs.acs.org/doi/10.1021/jacs.2c09477.

Additional graphs of experimental data including *ex situ* XRD of synthesized α-MnO_2 and cycled α-MnO_2 cathodes; detailed EELS, STEM, and HREM images of cycled electrodes; operando EXAFS data in *k*-space and EXAFS data of beamline standards; experimental results of Zn−Zn symmetric cells; 10-cycle *ex situ* XRD results of α-MnO_2 cathodes; illustrations of reference material structures and viscosity measurement results; and *ex situ* quantitative XRD analysis results, XANES-LCF results, and EXAFS fitting results (PDF)

https://doi.org/10.1021/jacs.2c09477
J. Am. Chem. Soc. 2022, 144, 23405−23420

AUTHOR INFORMATION

Corresponding Author

Kenneth J. Takeuchi − *Institute for Energy Sustainability and Equity, Stony Brook University, Stony Brook, New York 11794, United States; Department of Materials Science and Chemical Engineering and Department of Chemistry, Stony Brook University, Stony Brook, New York 11794, United States; Interdisciplinary Science Department, Brookhaven National Laboratory, Upton, New York 11973, United States;* orcid.org/0000-0001-8129-444X; Email: kenneth.takeuchi.1@stonybrook.edu

Authors

Daren Wu − *Institute for Energy Sustainability and Equity, Stony Brook University, Stony Brook, New York 11794, United States; Department of Materials Science and Chemical Engineering, Stony Brook University, Stony Brook, New York 11794, United States;* orcid.org/0000-0001-7947-9066

Lisa M. Housel − *Institute for Energy Sustainability and Equity, Stony Brook University, Stony Brook, New York 11794, United States; Interdisciplinary Science Department, Brookhaven National Laboratory, Upton, New York 11973, United States;* orcid.org/0000-0001-8429-5480

Steven T. King − *Institute for Energy Sustainability and Equity, Stony Brook University, Stony Brook, New York 11794, United States; Department of Chemistry, Stony Brook University, Stony Brook, New York 11794, United States;* orcid.org/0000-0001-8913-0423

Zachary R. Mansley − *Interdisciplinary Science Department, Brookhaven National Laboratory, Upton, New York 11973, United States; Department of Condensed Matter Physics and Materials Science, Brookhaven National Laboratory, Upton, New York 11973, United States;* orcid.org/0000-0002-1284-6316

Nahian Sadique − *Institute for Energy Sustainability and Equity, Stony Brook University, Stony Brook, New York 11794, United States; Department of Chemistry, Stony Brook University, Stony Brook, New York 11794, United States;* orcid.org/0000-0002-6830-9237

Yimei Zhu − *Department of Materials Science and Chemical Engineering, Stony Brook University, Stony Brook, New York 11794, United States; Department of Condensed Matter Physics and Materials Science, Brookhaven National Laboratory, Upton, New York 11973, United States;* orcid.org/0000-0002-1638-7217

Lu Ma − *National Synchrotron Light Source II, Brookhaven National Laboratory, Upton, New York 11973, United States*

Steven N. Ehrlich − *National Synchrotron Light Source II, Brookhaven National Laboratory, Upton, New York 11973, United States*

Hui Zhong − *National Synchrotron Light Source II, Brookhaven National Laboratory, Upton, New York 11973, United States*

Esther S. Takeuchi − *Institute for Energy Sustainability and Equity, Stony Brook University, Stony Brook, New York 11794, United States; Department of Materials Science and Chemical Engineering and Department of Chemistry, Stony Brook University, Stony Brook, New York 11794, United States; Interdisciplinary Science Department, Brookhaven National Laboratory, Upton, New York 11973, United States;* orcid.org/0000-0001-8518-1047

Amy C. Marschilok − *Institute for Energy Sustainability and Equity, Stony Brook University, Stony Brook, New York 11794, United States; Department of Materials Science and Chemical Engineering and Department of Chemistry, Stony Brook University, Stony Brook, New York 11794, United States; Interdisciplinary Science Department, Brookhaven National Laboratory, Upton, New York 11973, United States;* orcid.org/0000-0001-9174-0474

David C. Bock − *Institute for Energy Sustainability and Equity, Stony Brook University, Stony Brook, New York 11794, United States; Interdisciplinary Science Department, Brookhaven National Laboratory, Upton, New York 11973, United States;* orcid.org/0000-0002-2387-7791

Lei Wang − *Institute for Energy Sustainability and Equity, Stony Brook University, Stony Brook, New York 11794, United States; Interdisciplinary Science Department, Brookhaven National Laboratory, Upton, New York 11973, United States;* orcid.org/0000-0002-6348-8344

Complete contact information is available at: https://pubs.acs.org/10.1021/jacs.2c09477

Author Contributions

[▽]D.W. and L.M.H. contributed equally.

Notes

The authors declare no competing financial interest.

ACKNOWLEDGMENTS

This work was supported as part of the Center for Mesoscale Transport Properties, an Energy Frontier Research Center supported by the U.S. Department of Energy, Office of Science, Basic Energy Sciences via grant #DE-SC0012673. The microscopy work was conducted at the Brookhaven National Laboratory, which is supported by the U.S. Department of Energy, Basic Energy Sciences, Materials Science and Engineering Division, under Contract No. DE-SC0012704. The synchrotron measurements were conducted at the X-ray Powder Diffraction (XPD, 28-ID-2) and the Quick X-ray Absorption and Scattering (QAS, 7-BM) of the National Synchrotron Light Source II (NSLS-II), which is a U.S. DOE Office of Science Facility, at Brookhaven National Laboratory under Contract No. DE-SC0012704. The electron microscopy resource at Brookhaven National Laboratory (BNL) was sponsored by the US DOE-BES, Materials Sciences and Engineering Division, under Contract No. DE-SC0012704. E.S.T. acknowledges support from the William and Jane Knapp Chair in Energy and the Environment. L.M.H. acknowledges financial support from a BNL Laboratory Directed Research and Development (LDRD) project.

REFERENCES

(1) Blanc, L. E.; Kundu, D.; Nazar, L. F. Scientific Challenges for the Implementation of Zn-Ion Batteries. *Joule* **2020**, *4*, 771−799.

(2) Ingale, N. D.; Gallaway, J. W.; Nyce, M.; Couzis, A.; Banerjee, S. Rechargeability and economic aspects of alkaline zinc-manganese dioxide cells for electrical storage and load leveling. *J. Power Sources* **2015**, *276*, 7−18.

(3) Lim, M. B.; Lambert, T. N.; Chalamala, B. R. Rechargeable alkaline zinc-manganese oxide batteries for grid storage: Mechanisms, challenges and developments. *Mater. Sci. Eng., R* **2021**, *143*, 100593.

(4) Yamamoto, T.; Shoji, T. Rechargeable Zn|ZnSO4|MnO2-type cells. *Inorg. Chim. Acta* **1986**, *117*, L27−L28.

(5) Xu, C.; Chiang, S. W.; Ma, J.; Kang, F. Investigation on zinc ion storage in alpha manganese dioxide for zinc ion battery by

electrochemical impedance spectrum. *J. Electrochem. Soc.* **2013**, *160*, A93.
(6) Alfaruqi, M. H.; Mathew, V.; Gim, J.; Gim, J.; Kim, S.; Kim, S.; Song, J.; Song, J.; Baboo, J.; Baboo, J. P.; Choi, S.; Choi, S. H.; Kim, J. Electrochemically induced structural transformation in a γ-MnO2 cathode of a high capacity zinc-ion battery system. *Chem. Mater.* **2015**, *27*, 3609.
(7) Lee, B.; Seo, H. R.; Lee, H. R.; Yoon, C. S.; Kim, J. H.; Chung, K. Y.; Cho, B. W.; Oh, S. H. Critical Role of pH Evolution of Electrolyte in the Reaction Mechanism for Rechargeable Zinc Batteries. *ChemSusChem* **2016**, *9*, 2948−2956.
(8) Xu, C.; Li, B.; Du, H.; Kang, F. Energetic Zinc Ion Chemistry: The Rechargeable Zinc Ion Battery. *Angew. Chem., Int. Ed.* **2012**, *51*, 933−935.
(9) Sun, W.; Wang, F.; Hou, S.; Yang, C.; Fan, X.; Ma, Z.; Gao, T.; Han, F.; Hu, R.; Zhu, M.; Wang, C. Zn/MnO2 Battery Chemistry With H+ and Zn2+ Coinsertion. *J. Am. Chem. Soc.* **2017**, *139*, 9775−9778.
(10) Oberholzer, P.; Tervoort, E.; Bouzid, A.; Pasquarello, A.; Kundu, D. Oxide versus Nonoxide Cathode Materials for Aqueous Zn Batteries: An Insight into the Charge Storage Mechanism and Consequences Thereof. *ACS Appl. Mater. Interfaces* **2019**, *11*, 674−682.
(11) Liu, W.; Zhang, X.; Huang, Y.; Jiang, B.; Chang, Z.; Xu, C.; Kang, F. β-MnO2 with proton conversion mechanism in rechargeable zinc ion battery. *J. Energy Chem.* **2021**, *56*, 365−373.
(12) Lee, B.; Yoon, C. S.; Lee, H. R.; Chung, K. Y.; Cho, B. W.; Oh, S. H. Electrochemically-induced reversible transition from the tunneled to layered polymorphs of manganese dioxide. *Sci. Rep.* **2015**, *4*, No. 6066.
(13) Lee, B.; Lee, H. R.; Kim, H.; Chung, K. Y.; Cho, B. W.; Oh, S. H. Elucidating the intercalation mechanism of zinc ions into α-MnO2 for rechargeable zinc batteries. *Chem. Commun.* **2015**, *51*, 9265−9268.
(14) Pan, H.; Shao, Y.; Yan, P.; Cheng, Y.; Han, K. S.; Nie, Z.; Wang, C.; Yang, J.; Li, X.; Bhattacharya, P.; et al. Reversible aqueous zinc/manganese oxide energy storage from conversion reactions. *Nat. Energy* **2016**, *1*, 16039.
(15) Zhang, N.; Cheng, F.; Liu, Y.; Zhao, Q.; Lei, K.; Chen, C.; Liu, X.; Chen, J. Cation-Deficient Spinel ZnMn2O4 Cathode in Zn(CF3SO3)2 Electrolyte for Rechargeable Aqueous Zn-Ion Battery. *J. Am. Chem. Soc.* **2016**, *138*, 12894−12901.
(16) Zhang, N.; Cheng, F.; Liu, J.; Wang, L.; Long, X.; Liu, X.; Li, F.; Chen, J. Rechargeable aqueous zinc-manganese dioxide batteries with high energy and power densities. *Nat. Commun.* **2017**, *8*, No. 405.
(17) Huang, Y.; Mou, J.; Liu, W.; Wang, X.; Dong, L.; Kang, F.; Xu, C. Novel Insights into Energy Storage Mechanism of Aqueous Rechargeable Zn/MnO2 Batteries with Participation of Mn2+. *Nano-Micro Lett.* **2019**, *11*, 49.
(18) Gao, X.; Wu, H.; Li, W.; Tian, Y.; Zhang, Y.; Wu, H.; Yang, L.; Zou, G.; Hou, H.; Ji, X. H+-Insertion Boosted α-MnO2 for an Aqueous Zn-Ion Battery. *Small* **2020**, *16*, No. 1905842.
(19) Huang, J.; Wang, Z.; Hou, M.; Dong, X.; Liu, Y.; Wang, Y.; Xia, Y. Polyaniline-intercalated manganese dioxide nanolayers as a high-performance cathode material for an aqueous zinc-ion battery. *Nat. Commun.* **2018**, *9*, No. 2906.
(20) Lei, J.; Yao, Y.; Wang, Z.; Lu, Y.-C. Towards high-areal-capacity aqueous zinc−manganese batteries: promoting MnO2 dissolution by redox mediators. *Energy Environ. Sci.* **2021**, *14*, 4418−4426.
(21) Guo, X.; Zhou, J.; Bai, C.; Li, X.; Fang, G.; Liang, S. Zn/MnO2 battery chemistry with dissolution-deposition mechanism. *Materials Today Energy* **2020**, *16*, No. 100396.
(22) Wu, D.; Housel, L. M.; Kim, S. J.; Sadique, N.; Quilty, C. D.; Wu, L.; Tappero, R.; Nicholas, S. L.; Ehrlich, S.; Zhu, Y.; et al. Quantitative temporally and spatially resolved X-ray fluorescence microprobe characterization of the manganese dissolution-deposition mechanism in aqueous Zn/α-MnO2 batteries. *Energy Environ. Sci.* **2020**, *13*, 4322−4333.
(23) Kim, S. J.; Wu, D.; Housel, L. M.; Wu, L.; Takeuchi, K. J.; Marschilok, A. C.; Takeuchi, E. S.; Zhu, Y. Toward the Understanding of the Reaction Mechanism of Zn/MnO2 Batteries Using Non-alkaline Aqueous Electrolytes. *Chem. Mater.* **2021**, *33*, 7283−7289.
(24) Chao, D.; Zhou, W.; Ye, C.; Zhang, Q.; Chen, Y.; Gu, L.; Davey, K.; Qiao, S.-Z. An Electrolytic Zn−MnO2 Battery for High-Voltage and Scalable Energy Storage. *Angew. Chem., Int. Ed.* **2019**, *58*, 7823−7828.
(25) Fitz, O.; Bischoff, C.; Bauer, M.; Gentischer, H.; Birke, K. P.; Henning, H.-M.; Biro, D. Electrolyte Study with in Operando pH Tracking Providing Insight into the Reaction Mechanism of Aqueous Acidic Zn//MnO2 Batteries. *ChemElectroChem* **2021**, *8*, 3553−3566.
(26) Mateos, M.; Harris, K. D.; Limoges, B.; Balland, V. Nanostructured Electrode Enabling Fast and Fully Reversible MnO2-to-Mn2+ Conversion in Mild Buffered Aqueous Electrolytes. *ACS Applied Energy Materials* **2020**, *3*, 7610−7618.
(27) Wang, M.; Zheng, X.; Zhang, X.; Chao, D.; Qiao, S.-Z.; Alshareef, H. N.; Cui, Y.; Chen, W. Opportunities of Aqueous Manganese-Based Batteries with Deposition and Stripping Chemistry. *Adv. Energy Mater.* **2021**, *11*, No. 2002904.
(28) Yang, J.; Cao, J.; Peng, Y.; Yang, W.; Barg, S.; Liu, Z.; Kinloch, I. A.; Bissett, M. A.; Dryfe, R. A. W. Unravelling the Mechanism of Rechargeable Aqueous Zn−MnO2 Batteries: Implementation of Charging Process by Electrodeposition of MnO2. *ChemSusChem* **2020**, *13*, 4103−4110.
(29) Lee, B.; Choi, J.; Lee, M.; Han, S.; Jeong, M.; Yim, T.; Oh, S. H. Unraveling the critical role of Zn-phyllomanganates in zinc ion batteries. *J. Mater. Chem. A* **2021**, *9*, 13950−13957.
(30) Moon, H.; Ha, K.-H.; Park, Y.; Lee, J.; Kwon, M.-S.; Lim, J.; Lee, M.-H.; Kim, D.-H.; Choi, J. H.; Choi, J.-H.; Lee, K. T. Direct Proof of the Reversible Dissolution/Deposition of Mn2+/Mn4+ for Mild-Acid Zn-MnO2 Batteries with Porous Carbon Interlayers. *Adv. Sci.* **2021**, *8*, No. 2003714.
(31) Xie, C.; Li, T.; Deng, C.; Song, Y.; Zhang, H.; Li, X. A highly reversible neutral zinc/manganese battery for stationary energy storage. *Energy Environ. Sci.* **2020**, *13*, 135−143.
(32) Mateos, M.; Makivic, N.; Kim, Y.-S.; Limoges, B.; Balland, V. Accessing the Two-Electron Charge Storage Capacity of MnO2 in Mild Aqueous Electrolytes. *Adv. Energy Mater.* **2020**, *10*, No. 2000332.
(33) Zeng, X.; Liu, J.; Mao, J.; Hao, J.; Wang, Z.; Zhou, S.; Ling, C. D.; Guo, Z. Toward a Reversible Mn4+/Mn2+ Redox Reaction and Dendrite-Free Zn Anode in Near-Neutral Aqueous Zn/MnO2 Batteries via Salt Anion. *Chemistry* **2020**, *10*, No. 1904163.
(34) Bischoff, C. F.; Fitz, O. S.; Burns, J.; Bauer, M.; Gentischer, H.; Birke, K. P.; Henning, H.-M.; Biro, D. Revealing the Local pH Value Changes of Acidic Aqueous Zinc Ion Batteries with a Manganese Dioxide Electrode during Cycling. *J. Electrochem. Soc.* **2020**, *167*, No. 020545.
(35) Luo, J.; Zhu, H. T.; Fan, H. M.; Liang, J. K.; Shi, H. L.; Rao, G. H.; Li, J. B.; Du, Z. M.; Shen, Z. X. Synthesis of Single-Crystal Tetragonal α-MnO2 Nanotubes. *J. Phys. Chem. C* **2008**, *112*, 12594−12598.
(36) Huang, J.; Yan, S.; Wu, D.; Housel, L.; Hu, X.; Hwang, S.; Wang, L.; Tong, X.; Wu, L.; Zhu, Y.; et al. Potassium-Containing α-MnO2 Nanotubes: The Impact of Hollow Regions on Electrochemistry. *J. Electrochem. Soc.* **2021**, *168*, No. 090559.
(37) Toby, B. H.; Von Dreele, R. B. GSAS-II: the genesis of a modern open-source all purpose crystallography software package. *J. Appl. Crystallogr.* **2013**, *46*, 544−549.
(38) Lee, D. D.; Seung, H. S. Learning the parts of objects by non-negative matrix factorization. *Nature* **1999**, *401*, 788−791.
(39) Long, C. J.; Bunker, D.; Li, X.; Karen, V. L.; Takeuchi, I. Rapid identification of structural phases in combinatorial thin-film libraries using x-ray diffraction and non-negative matrix factorization. *Rev. Sci. Instrum.* **2009**, *80*, 103902.
(40) Zhang, X.; Hui, Z.; King, S.; Wang, L.; Ju, Z.; Wu, J.; Takeuchi, K. J.; Marschilok, A. C.; West, A. C.; Takeuchi, E. S.; Yu, G. Tunable Porous Electrode Architectures for Enhanced Li-Ion Storage Kinetics in Thick Electrodes. *Nano Lett.* **2021**, *21*, 5896−5904.

https://doi.org/10.1021/jacs.2c09477
J. Am. Chem. Soc. 2022, 144, 23405−23420

(41) Ravel, B.; Newville, M. ATHENA, ARTEMIS, HEPHAESTUS: data analysis for X-ray absorption spectroscopy using IFEFFIT. *J. Synchrotron Radiat.* **2005**, *12*, 537−541.
(42) Rehr, J. J.; Mustre de Leon, J.; Zabinsky, S. I.; Albers, R. C. Theoretical x-ray absorption fine structure standards. *J. Am. Chem. Soc.* **1991**, *113*, 5135−5140.
(43) Shinagawa, T.; Watanabe, M.; Mori, T.; Tani, J.-i.; Chigane, M.; Izaki, M. Oriented Transformation from Layered Zinc Hydroxides to Nanoporous ZnO: A Comparative Study of Different Anion Types. *Inorg. Chem.* **2018**, *57*, 13137−13149.
(44) Jo, J. H.; Aniskevich, Y.; Kim, J.; Choi, J. U.; Kim, H. J.; Jung, Y. H.; Ahn, D.; Jeon, T.-Y.; Lee, K.-S.; Song, S. H.; et al. New Insight on Open-Structured Sodium Vanadium Oxide as High-Capacity and Long Life Cathode for Zn−Ion Storage: Structure, Electrochemistry, and First-Principles Calculation. *Adv. Energy Mater.* **2020**, *10*, No. 2001595.
(45) Saravanan, M. S.; Babu, S.; Sivaprasad, K.; Jagannatham, M. Science; Technology. Techno-economics of carbon nanotubes produced by open air arc discharge method. *Int. J. Eng. Sci.* **2010**, *2*, 100−108.
(46) Nuffield, E. W. *X-ray Diffraction Methods*; Wiley, 1966.
(47) Post, J. E.; McKeown, D. A.; Heaney, P. J. Raman spectroscopy study of manganese oxides: Tunnel structures. *Am. Mineral.* **2020**, *105*, 1175−1190.
(48) Post, J. E.; McKeown, D. A.; Heaney, P. J. Raman spectroscopy study of manganese oxides: Layer structures. *Am. Mineral.* **2021**, *106*, 351−366.
(49) Lee, B.; Yoon, C. S.; Lee, H. R.; Chung, K. Y.; Cho, B. W.; Oh, S. H. Electrochemically-induced reversible transition from the tunneled to layered polymorphs of manganese dioxide. *Scientific Reports* **2014**, *4*, No. 6066.
(50) Kim, S. J.; Wu, D.; Housel, L. M.; Wu, L.; Takeuchi, K. J.; Marschilok, A. C.; Takeuchi, E. S.; Zhu, Y. Toward the Understanding of the Reaction Mechanism of Zn/MnO_2 Batteries Using Non-alkaline Aqueous Electrolytes. *Chem. Mater.* **2021**, *33*, 7283−7289.
(51) Post, J. E.; Veblen, D. R. Crystal structure determinations of synthetic sodium, magnesium, and potassium birnessite using TEM and the Rietveld method. *Am. Mineral.* **1990**, *75*, 477−489.
(52) Silvester, E.; Manceau, A.; Drits, V. A. Structure of synthetic monoclinic Na-rich birnessite and hexagonal birnessite: II. Results from chemical studies and EXAFS spectroscopy %. *J. Am. Mineral.* **1997**, *82*, 962−978.
(53) Lopano, C. L.; Heaney, P. J.; Post, J. E.; Hanson, J.; Komarneni, S. Time-resolved structural analysis of K- and Ba-exchange reactions with synthetic Na-birnessite using synchrotron X-ray diffraction. *Am. Mineral.* **2007**, *92*, 380−387.
(54) Patridge, C. J. Operando XAFS on Hydrated Calcium Vanadium Bronze Cathode for Aqueous Zn-ion Storage. *ChemPhysChem* **2022**, *23*, e202100674.
(55) Nam, K.-W.; Kim, M. G.; Kim, K.-B. In Situ Mn K-edge X-ray Absorption Spectroscopy Studies of Electrodeposited Manganese Oxide Films for Electrochemical Capacitors. *J. Phys. Chem. C* **2007**, *111*, 749−758.
(56) Webb, S. M.; Tebo, B. M.; Bargar, J. R. Structural characterization of biogenic Mn oxides produced in seawater by the marine bacillus sp. strain SG-1. *Am. Mineral.* **2005**, *90*, 1342−1357.
(57) Huang, J.; Housel, L. M.; Quilty, C. D.; Brady, A. B.; Smith, P. F.; Abraham, A.; Dunkin, M. R.; Lutz, D. M.; Zhang, B.; Takeuchi, E. S.; et al. Capacity retention for (de)lithiation of silver containing α-MnO2: Impact of structural distortion and transition metal dissolution. *J. Electrochem. Soc.* **2018**, *165*, A2849−A2858.
(58) Fernando, D. R.; Mizuno, T.; Woodrow, I. E.; Baker, A. J. M.; Collins, R. N. Characterization of foliar manganese (Mn) in Mn (hyper)accumulators using X-ray absorption spectroscopy. *New Phytol.* **2010**, *188*, 1014−1027.
(59) Chen, Y.; Fulton, J. L.; Partenheimer, W. A XANES and EXAFS Study of Hydration and Ion Pairing in Ambient Aqueous MnBr2 Solutions. *J. Solution Chem.* **2005**, *34*, 993−1007.
(60) Rehr, J. J.; Albers, R. C. Theoretical approaches to x-ray absorption fine structure. *Rev. Mod. Phys.* **2000**, *72*, 621−654.
(61) Yang, J.; Cao, J.; Peng, Y.; Yang, W.; Barg, S.; Liu, Z.; Kinloch, I. A.; Bissett, M. A.; Dryfe, R. A. W. Unravelling the Mechanism of Rechargeable Aqueous Zn−MnO2 Batteries: Implementation of Charging Process by Electrodeposition of MnO2. *ChemSusChem* **2020**, *13*, 4103−4110.
(62) Frenkel, A. I.; Kleifeld, O.; Wasserman, S. R.; Sagi, I. Phase speciation by extended x-ray absorption fine structure spectroscopy. *J. Chem. Phys.* **2002**, *116*, 9449−9456.
(63) Vicat, J.; Fanchon, E.; Strobel, P.; Tran Qui, D. The structure of K1.33Mn8O16 and cation ordering in hollandite-type structures. *Acta Crystallogr. B* **1986**, *42*, 162−167.
(64) Wadsley, A. D. The crystal structure of chalcophanite, ZnMn3O7.3H2O. *Acta Crystallogr.* **1955**, *8*, 165−172.
(65) Belli, M.; Scafati, A.; Bianconi, A.; Mobilio, S.; Palladino, L.; Reale, A.; Burattini, E. X-ray absorption near edge structures (XANES) in simple and complex Mn compounds. *Solid State Commun.* **1980**, *35*, 355−361.
(66) Bricker, O. Some stability relations in the system Mn-O2-H2O at 25° and one atmosphere total pressure. *Am. Mineral.* **1965**, *50*, 1296−1354.
(67) Stoševski, I.; Bonakdarpour, A.; Fang, B.; Lo, P.; Wilkinson, D. P. Formation of MnxZny(OH)zSO4·5H2O − not intercalation of Zn − is the basis of the neutral MnO2/Zn battery first discharge reaction. *Electrochim. Acta* **2021**, *390*, No. 138852.
(68) Huang, J.; Hu, X.; Brady, A. B.; Wu, L.; Zhu, Y.; Takeuchi, E. S.; Marschilok, A. C.; Takeuchi, K. J. Unveiling the Structural Evolution of Ag1.2Mn8O16 under Coulombically Controlled (De)-Lithiation. *Chem. Mater.* **2018**, *30*, 366−375.
(69) Sun, W.; Wang, F.; Zhang, B.; Zhang, M.; Küpers, V.; Ji, X.; Theile, C.; Bieker, P.; Xu, K.; Wang, C.; et al. A rechargeable zinc-air battery based on zinc peroxide chemistry. *Science* **2021**, *371*, 46−51.
(70) Zhang, Y.; Zhang, N.; Liu, Y.; Chen, Y.; Huang, H.; Wang, W.; Xu, X.; Li, Y.; Fan, F.; Ye, J.; et al. Homogeneous solution assembled Turing structures with near zero strain semi-coherence interface. *Nat. Commun.* **2022**, *13*, No. 2942.
(71) Artamonova, I. V.; Gorichev, I.; Godunov, E. Kinetics of manganese oxides dissolution in sulphuric acid solutions containing oxalic acid. *Engineering* **2013**, *05*, 714−719.
(72) Barton, J. L.; Milshtein, J. D.; Hinricher, J. J.; Brushett, F. R. Quantifying the impact of viscosity on mass-transfer coefficients in redox flow batteries. *J. Power Sources* **2018**, *399*, 133−143.

https://doi.org/10.1021/jacs.2c09477
J. Am. Chem. Soc. 2022, 144, 23405−23420